

# Photometric and polarimetric observations of fast declining Type II supernovae 2013hj and 2014G

Subhash Bose<sup>1,2\*</sup>, Brijesh Kumar<sup>1</sup>, Kuntal Misra<sup>1</sup>, Katsura Matsumoto<sup>3†</sup>,  
Brajesh Kumar<sup>4,1</sup>, Mridweeka Singh<sup>1</sup>, Daiki Fukushima<sup>3†</sup>, Miho Kawabata<sup>3†</sup>

<sup>1</sup>*Aryabhata Research Institute of Observational Sciences, Manora Peak, Nainital - 263002, India.*

<sup>2</sup>*Centre of Advance Study, Department of Physics, Kumaun University, Nainital - 263001, India.*

<sup>3</sup>*Osaka Kyoiku University, 4-698-1 Asahigaoka, Kashiwara, Osaka 582-8582*

<sup>4</sup>*Indian Institute of Astrophysics, Block-II, Koramangala, Bangalore - 560034, India.*

Accepted.....; Received .....

## ABSTRACT

We present broadband photometric and polarimetric observations of two type II supernovae (SNe) 2013hj and 2014G. SN 2014G is a spectroscopically classified type IIL event, which we also confirm photometrically as its light curve show characteristic features (plateau slope of  $2.55 \text{ mag } (100 \text{ d})^{-1}$  in  $V$ -band and duration of  $\sim 77\text{d}$ ) of a generic IIL SN. On the other hand SN 2013hj also shows high plateau decline rate of  $1.5 \text{ mag } (100 \text{ d})^{-1}$  in  $V$ -band, similar to SNe IIL, but marginally lower than SNe IIL template light curves. Our high cadence photometric observations of SNe 2013hj and 2014G enables us to cover all characteristic phases up to radioactive tail of optical light curves. Broadband polarimetric observations reveal some polarization in SN 2013hj with subtle enhancement as SN evolves towards plateau end, however the polarization angle remains constant throughout the evolution. This characteristic is consistent with the idea that the evolving SN with recombining hydrogen envelope is slowly revealing more asymmetric central region of explosion. Modelling of bolometric light curve yields a progenitor mass of  $\sim 11M_{\odot}$  with a radius of  $\sim 700R_{\odot}$  for SN 2013hj, while for SN 2014G model estimated progenitor mass is  $\sim 9M_{\odot}$  with a radius of  $\sim 630R_{\odot}$ , both having a typical energy budget of  $\sim 2 \times 10^{51}$  erg.

**Key words:** supernovae: general – supernovae: individual: SN 2013hj, SN 2014G – galaxies: individual: MCG -02-24-3, NGC 3448

## 1 INTRODUCTION

Core-Collapse SNe (CCSNe) originate from massive stars with  $M_{ZAMS} > 8M_{\odot}$  (Burrows 2013) which at the end of nuclear burning phase, having insufficient thermal energy start to collapse under self gravity. The massive core overcomes the electron degeneracy state following which process of neutronization takes place releasing large amount of energetic neutrinos which helps drive the explosion. CCSNe are sub classified into Hydrogen rich (Type II) and hydrogen deficient (Type I) SNe. The retention of significant amount of Hydrogen in SNe II at the time of explosion is visible as characteristic Balmer emissions in their spectra.

CCSNe are further divided in various sub types (see Filippenko 1997, for a review of SN classifications). Among these the most common sub-type is IIP which constitutes

$\sim 60\%$  of all CCSNe (Li et al. 2011). SNe IIP has extended hydrogen envelope which is left almost fully ionized at the time of shock breakout. As expanding envelope cools down, the ionized envelope starts to recombine with recombination front moving inward through the ejecta which is responsible for a sustained plateau of almost constant brightness for  $\sim 80 - 100$  days. At the end of recombination phase, SNe IIP experience rapid drop in luminosity settling onto a slow declining tail phase which is powered by gamma rays emitted from the radioactive decay of  $^{56}\text{Co}$  to  $^{56}\text{Fe}$  which in turn depends upon the amount of short lived radioactive  $^{56}\text{Ni}$  synthesized in explosion.

According to historical classification based on the light curve properties (Barbon et al. 1979), fast declining counterpart of type IIPs are SNe IIL, which are supposed to show almost a linear decline in the light curve until it reaches the tail phase, without any sort of flattening during early phases of light curve. Over time it has been realized that such events are extremely rare that could fit in the criteria of SNe IIL.

\* e-mail: email@subhashbose.com, bose@aries.res.in

† Author's contribution is for SN 2013hj.

Studies by [Anderson et al. \(2014\)](#) and [Sanders et al. \(2015\)](#) on a large sample of SNe II disapprove existence of any bimodality in light curve properties which can be grouped into distinct subclasses. Rather they found a continuum in light curve slopes and physical parameters. Moreover now it is also believed that a steep declining plateau-nebular transition like phase can be detected even in typical SNe IIL if they are observed long enough. The plateau slope of SNe II light curves are primarily governed by the amount of hydrogen present in the ejecta. As in the case of SNe IIP where the hydrogen content is high enough with an extended envelope, the energy deposited instantaneously from shock and also from the initial decay of  $^{56}\text{Ni}$  is released slowly over a longer period of time, which sustain the flat plateau phase. On the contrary, if the amount of intact hydrogen is relatively less, then energy will be released at a faster rate resulting in a fast declining light curve but with a brighter initial peak luminosity. Considering vast diversity of progenitor properties ([Smartt 2009](#)), variable amount of hydrogen mass intact in the ejecta would give rise to a continuum distribution of light curve slopes. [Faran et al. \(2014\)](#) proposed a criteria to reestablish SNe IIL classification, according to which a SN with a decline of 0.5 mag in  $V$ -band light curve during first 50 days would qualify as a type IIL. However this criteria is a bit too rigid for IIL classification as it will classify more than 50% of all Type II SNe as Type IIL considering the sample of [Anderson et al. \(2014\)](#). Therefore, rather than using this criteria we use SNe IIL light curve template presented by [Faran et al. \(2014\)](#) for the purpose of classification. It is also to be noted, that even by following scheme of template matching, many of the earlier studies which comprises of collective sample of SNe IIP may also include some reclassified SNe IIL as well.

Extensive theoretical and numerical attempts have been made to understand progenitor properties and relate them with other observable parameters of explosion ([Litvinova & Nadezhin 1985](#); [Arnett & Fu 1989](#); [Hamuy 2003](#)). Stellar evolutionary models suggest that these SNe can originate from red supergiant (RSG) stars of masses  $\sim 9 - 25M_{\odot}$  (e.g. [Heger et al. 2003](#)). However, progenitors directly identified from pre-SN archival *HST* images for a decent number of IIP SNe suggest an upper mass limit of  $16.5 \pm 1.5 M_{\odot}$  ([Smartt et al. 2009](#)). One of the many proposed explanation for the lack of high mass RSG progenitors is that stars above  $17M_{\odot}$  may end up into IIL or IIn SNe ([Smartt 2009](#)).

Extragalactic SNe are spatially unresolvable and hence its difficult to address structure and geometry of explosion. Polarimetric observations have proved to be a valuable probe in investigating asymmetry of SN explosion. In SNe the source of polarization is primarily the geometry of electron scattering atmosphere within the ejecta. Any asymmetry in this envelope would give rise to net polarization of observed light. CCSNe are often found to show significant degree of polarization in optical and IR wavelengths ([Wang & Wheeler 1996](#); [Leonard et al. 2001](#); [Leonard & Filippenko 2001](#); [Wang et al. 2002a](#); [Pereyra et al. 2006](#)). SNe with hydrogen envelope stripped (Type Ib/c) or partially stripped (Type Iib or IIn) exhibit higher level of polarization as compared to SNe with intact H envelope like SNe IIP (typically about 0.5 - 0.8% polarization). The thick H envelope obscures the

observed asymmetry, whereas probing deeper towards the central part of the explosion, more polarization is observed implying higher degree of asymmetry in electron scattering atmosphere ([Leonard & Filippenko 2005](#)). However, in IIP SNe polarization enhancement is observed towards the end of plateau as SN starts to enter the nebular phase, where the hydrogen recombination is close to completion, and with decreasing opacity the inner asymmetric core is being revealed (e.g. SN 2004dj; [Leonard et al. 2006](#)). Generally a moderate asphericity of  $\sim 20\%$  would result in a linear polarization of  $\sim 1\%$  ([Leonard & Filippenko 2005](#)). Besides asphericity in electron scattering atmosphere, some amount of polarization may also originate from scattering by dust environment ([Wang & Wheeler 1996](#)), clumps in ejecta, asymmetric distribution of radioactive  $^{56}\text{Ni}$  ([Chugai 2006](#)) or asymmetric ionization of outer envelope due to shock produced in CSM interaction.

The first broadband polarimetric observation was done for SN 1987A ([Barrett 1988](#)) demonstrating significant polarization and its time evolution. Late time *HST* observations of spatially resolved ejecta revealed elongation in a direction consistent to the polarization angle inferred from polarimetry ([Wang et al. 2002b](#)), which validated our understanding to use polarimetry as a probe for SN explosion geometry. SNe 1999em and 2004dj are extremely well studied and observed spectropolarimetrically, which provided detailed insight on the nature of these explosions ([Leonard et al. 2001, 2006](#)). While spectropolarimetry has advantage of wavelength resolved polarization information, on the other hand broadband polarimetry is useful to extract overall polarimetric information and infer any asymmetry without the requirement of bright SN or powerful observational resources.

In this work we present broadband photometric and polarimetric observations of two fast declining type II SNe 2013hj and 2014G. A brief introduction of these events is given in Section 1.1. This paper is organized as follows. In Section 2 we describe photometric and polarimetric observations and data reduction procedure. Adopted distance and estimated extinction values for both the SNe are discussed in Section 3. In Section 4 we analyze photometric light curve properties of SNe 2013hj and 2014G and compare with other SNe II to establish its position in Type II diversity. In this section we also estimate  $^{56}\text{Ni}$  mass from computed bolometric light curves. The explosion parameters and progenitor properties are estimated by modelling the light curve, which are described in Section 5. Polarimetric analysis and its temporal evolution is discussed in Section 6. Finally in Section 7 we summarize the results obtained in this work.

## 1.1 SNe 2013hj and 2014G

SNe 2013hj and 2014G, both are moderately bright events which have been detected very young. SN 2013hj was discovered on December 12.3 UTC, 2013 by [Antezana et al. \(2013\)](#) in the galaxy MCG -02-24-3 ( $\sim 30$  Mpc). Unfortunately there is no reported non-detection prior to SN explosion, which can be used to observationally constrain the explosion epoch. The classification spectrum from ASIAGO on December 13.1 UTC shows broad and very shallow  $H\alpha$  and  $H\beta$  P-Cygni profiles on top of featureless blue continuum. Comparison of this spectrum with well studied SNe tem-

plates, using GELATO (Harutyunyan et al. 2008) and SNID (Blondin & Tonry 2007), is found similar to type II SNe and matches best with SN 2012A spectrum at 2.6 day after explosion. Moreover, from visual comparison with other SNe II spectra (e.g., Valenti et al. 2014; Bose et al. 2015a) at early epochs, the December 13 spectrum looks no older than four days post explosion. Therefore, we adopt an explosion epoch (0d) of December 10.5 UTC, 2013 (JD = 2456637.0  $\pm$  1.5 days) for SN 2013hj.

SN 2014G was discovered on January 14.5 UTC, 2014 in NGC 3448 ( $\sim$  24 Mpc) and was reported in *CBAT Transient Object Followup Reports*<sup>1</sup>. They also reported an earlier faint detection ( $\sim$  17.4 mag) in CCD image taken on January 13.6 UTC with limiting magnitude of 18.5. Denisenko et al. (2014) reported last confirmed non-detection of the SN on January 10.9 UTC, 2014 up to a limiting magnitude of 19.4. Thus we adopt mid time between the first faintest detection and last non-detection as the explosion epoch (0d) for SN 2014G, which is January 12.2 UTC, 2014 (JD = 2456669.7  $\pm$  1.4 days). Ochner et al. (2014) reported optical spectrum taken on January 15.1 UTC, showing H $\alpha$  line with narrow H $\alpha$  emission and unusually strong He II line, which was found similar to type IIn SN 2013cj. However, it was again reclassified as type IIL by Enmae et al. (2014) from spectrum taken several weeks after peak. The basic parameters of these two SNe and their host galaxies are tabulated in Table. 1.

## 2 OBSERVATION AND DATA REDUCTION

### 2.1 Photometry

Broadband photometric observations of SNe 2013hj and 2014G have been carried out in *UBVRI* bands. Rigorous follow up observations for both the SNe were initiated soon after their discovery. The observations in the nebular phase continued until the objects went behind the Sun. High cadence monitoring was done using ARIES 104cm Sampurnanand Telescope (ST) and 130cm Devasthal Fast Optical Telescope (DFOT) located at Nainital, India. Additional *BVRI* data of SN 2013hj was also collected from 50cm telescope at Osaka Kyoiku University, Japan. *Swift* Ultraviolet optical telescope (UVOT) also observed SN 2014G for nearly a month in all six UVOT bands.

The routine data cleaning, reduction, extraction of light curve and field calibration to generate local standards follows the same procedure as outlined in Bose et al. (2013). Fig. 1 and Fig. 2 shows the field of SNe 2013hj and 2014G respectively. As seen in the figures both the SNe are fairly embedded in their host galaxies and the estimated SN flux measurements will be contaminated by the background specially during late phases. It is therefore necessary to correct for the host galaxy fluxes and in order to do so galaxy templates have been observed. Template images of the host galaxies in all five photometric bands were taken during 7 to 10 May 2015 when the SNe have faded much below the detection limit (at an age of  $\sim$  515 and  $\sim$  480 days for SN 2013hj and SN 2014G respectively). In order to do the template correction, we adopted aperture flux subtraction

**Table 1.** Parameters of SNe and their host galaxies.

Parameters	Value	Ref.
<b>SN 2013hj</b>		
<i>MCG -02-24-3:</i>		
Alternate name	PGC 025938	2
Type	SBcd	2
RA (J2000)	$\alpha = 09^{\text{h}}12^{\text{m}}06^{\text{s}}.7$	2
DEC (J2000)	$\delta = -15^{\circ}25'51''.9$	2
Abs. Magnitude	$M_B = -18.26$ mag	2
Distance	$D = 28.2 \pm 2.0$ Mpc	2
Distance modulus	$\mu = 32.25 \pm 0.15$ mag	
Heliocentric Velocity	$cz_{\text{helio}} = 2060 \pm 7$ km s $^{-1}$	2
<i>SN 2013hj:</i>		
RA (J2000)	$\alpha = 09^{\text{h}}12^{\text{m}}06^{\text{s}}.3$	3
DEC (J2000)	$\delta = -15^{\circ}25'46''.0$	
Galactocentric Location	6''5 W, 5''9 N	3
Time of explosion	$t_0 = 10.5$ December 2013 (UTC) (JD 2456637.0 $\pm$ 1.5 day)	1
Total reddening	$E(B - V) = 0.100 \pm 0.069$ mag	1
<b>SN 2014G</b>		
<i>NGC 3448:</i>		
Type	Sab	2
RA (J2000)	$\alpha = 10^{\text{h}}54^{\text{m}}39^{\text{s}}.4$	2
DEC (J2000)	$\delta = 54^{\circ}18'18''.8$	2
Abs. Magnitude	$M_B = -20.07$ mag	2
Distance	$D = 24.4 \pm 9.0$ Mpc	2
Distance modulus	$\mu = 31.94 \pm 0.80$ mag	
Heliocentric Velocity	$cz_{\text{helio}} = 1372 \pm 8$ km s $^{-1}$	4
<i>SN 2014G:</i>		
RA (J2000)	$\alpha = 10^{\text{h}}54^{\text{m}}34^{\text{s}}.1$	5
DEC (J2000)	$\delta = 54^{\circ}17'56''.9$	
Galactocentric Location	44''W, 20''N	5
Time of explosion	$t_0 = 12.2$ January 2014 (UTC) (JD 2456669.7 $\pm$ 1.4 day)	1
Total reddening	$E(B - V) = 0.254 \pm 0.072$ mag	1

(1) This paper; (2) HyperLEDA - <http://leda.univ-lyon1.fr> (Makarov et al. 2014); (3) Antezana et al. (2013); (4) Tully & Fisher (1988); (5) Denisenko et al. (2014)

method, in which the SN flux and host galaxy background flux (from the template image) is extracted using the same aperture and at the same exact same location. The SN fluxes are then subtracted by the estimated background flux resulting into true SN flux free from galaxy contamination. This entire process is achieved with a set of self written scripts which employs DAOPHOT within it. In principle, the technique of template image subtraction should be adopted for best results (Alard & Lupton 1998; Alard 2000). However, in this technique there are number of shortcoming with data obtained from small ground based telescopes. Stellar point spread function (PSF) may often be degraded in terms

<sup>1</sup> <http://www.cbata.harvard.edu/unconf/toconf.html>

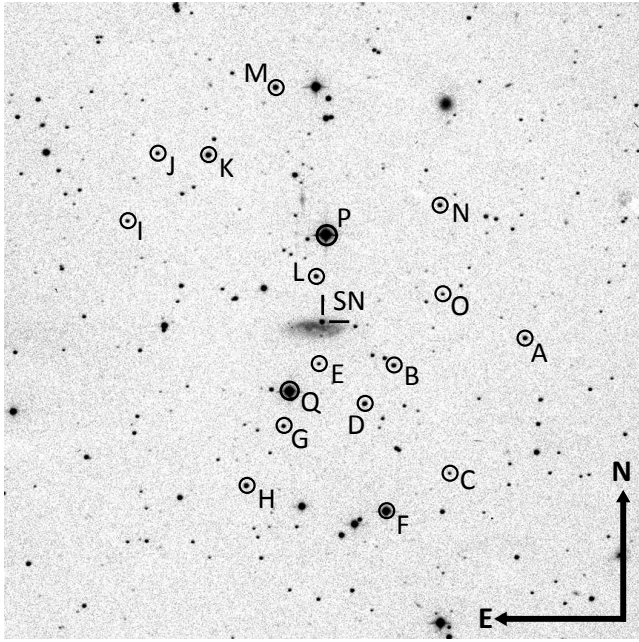


**Figure 1.** SN 2013hj in MCG -02-24-3. The  $V$ -band image taken from 104-cm ST covering a subsection of about  $11' \times 11'$  is shown. The secondary field standards are marked with circles.

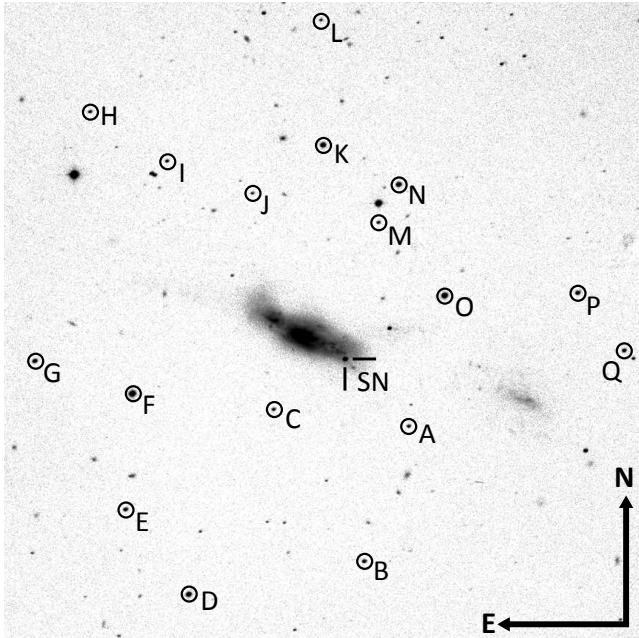


**Figure 2.** SN 2014G in NGC 3448. The  $V$ -band image taken from 104-cm ST covering a subsection of about  $11' \times 11'$  is shown. The secondary field standards are marked with circles.

of minor elongation and skewness due to defect in passive telescope optics, which may further vary depending on the telescope's altitude-azimuth. In such cases, PSF matching becomes non trivial and may leave behind significant and arbitrary residual in flux, resulting into larger errors in photometry. In our case, such defects are prevailing in several images when the SNe were observed at high zenith angles.

To standardize both the SNe fields, four Landolt (2009)

standard fields (PG 1323, PG 1633, SA 104 and SA 107) were observed on March 08 2014 from 104-cm ST under good photometric night and seeing (FWHM  $\sim 2''$  in  $V$  band) conditions. For determination of atmospheric extinction, multiple standard fields were observed with varying air masses. SNe fields were also observed during the same night, so that the derived transformation can be used to calibrate instrumental magnitudes of SNe. The obtained transformation equations with zero-point, color and atmospheric extinction coefficients are given as,

$$\begin{aligned}
 u &= U + (7.841 \pm 0.012) - (0.071 \pm 0.013) \cdot (U - B) \\
 &\quad + (0.660 \pm 0.034) \cdot X \\
 b &= B + (5.319 \pm 0.010) - (0.072 \pm 0.010) \cdot (B - V) \\
 &\quad + (0.402 \pm 0.020) \cdot X \\
 v &= V + (4.715 \pm 0.007) - (0.063 \pm 0.006) \cdot (B - V) \\
 &\quad + (0.247 \pm 0.014) \cdot X \\
 r &= R + (4.429 \pm 0.007) - (0.057 \pm 0.010) \cdot (V - R) \\
 &\quad + (0.259 \pm 0.024) \cdot X \\
 i &= I + (4.892 \pm 0.010) - (0.050 \pm 0.010) \cdot (V - I) \\
 &\quad + (0.117 \pm 0.015) \cdot X
 \end{aligned} \tag{1}$$

where  $ubvri$  are instrumental magnitudes corrected for time and aperture,  $UBVRI$  are standard magnitudes and  $X$  is the airmass. These transformation equations are applied to the SNe fields to calibrate 17 secondary standard stars in each of the fields of SNe 2013hj and 2014G. The secondary standards are marked in Fig. 1 and Fig. 2, and their calibrated magnitudes are listed in Table A1. The final photometry of SN 2013hj and SN 2014G are tabulated in Tables A2 and A3 respectively.

SN 2014G was also observed with UVOT (Romig et al. 2005) on board *Swift* spacecraft (Gehrels et al. 2004) in all six UVOT bands ( $uvw2$ ,  $uvm2$ ,  $uvw1$ ,  $uwu$ ,  $uwb$ ,  $uvw$ ). The UVOT photometry was obtained from *Swift* Optical/Ultraviolet Supernova Archive (SOUSA; Brown et al. 2014). The reduction procedure for UVOT photometry is based on Brown et al. (2009), which includes subtraction of background galaxy counts, and adopting the revised zero-points and time dependent sensitivity from Breeveld et al. (2011). The UVOT photometry for SN 2014G is presented in Table A3.

## 2.2 Polarimetry

Broadband polarimetric observations in  $R$ -band have been carried out for SNe 2013hj and 2014G using ARIES Imaging Polarimeter (AIMPOL; Rautela et al. 2004) mounted at 104cm ST. The unvignetted field of view of the CCD image is  $\sim 8'$  in diameter. Stellar FWHM is found to vary within 2 to 3 pixels, CCD read-noise and gain are  $7.0e^-$  and  $11.98 e^-/ADU$  respectively.

Bias correction and cosmic ray removal is done following usual procedure. The Wollaston prism splits light into ordinary and extraordinary rays and make it incident on the CCD. The corresponding stellar images are separated by  $\sim 28$  pixels along the north-south direction on the sky plane. Images are taken in four positions by rotating the half-wave plate through an angle  $\alpha = 0^\circ, 22.5^\circ, 45^\circ$  and  $67.5^\circ$ , and the corresponding reduced stokes parameters are

designated as  $q1$ ,  $u1$ ,  $q2$  and  $u2$  respectively and are determined as,

$$R(\alpha) = \frac{I_e(\alpha)/I_o(\alpha) - 1}{I_e(\alpha)/I_o(\alpha) + 1} = P \cos(2\theta - 4\alpha). \quad (2)$$

Here,  $I_o$  and  $I_e$  are the intensities of ordinary and extraordinary stellar images determined from standard aperture photometry.  $P$  is the fraction of linear polarization and  $\theta$  is the angle of polarization plane. Correction factor for nonuniform responsivity of (i) CCD pixels and (ii) system to orthogonal polarized beams, is also introduced as a ratio described by Ramaprakash et al. (1998),

$$\frac{F_o}{F_e} = \left[ \frac{I_o(0^\circ)}{I_e(45^\circ)} \times \frac{I_o(45^\circ)}{I_e(0^\circ)} \times \frac{I_o(22.5^\circ)}{I_e(67.5^\circ)} \times \frac{I_o(67.5^\circ)}{I_e(22.5^\circ)} \right]^{0.25}, \quad (3)$$

which are multiplied with  $I_e/I_o$  ratios in Eq. 2. The obtained  $q1$ ,  $u1$ ,  $q2$ ,  $u2$  values are fitted with *cosine* function to obtain  $P$  and  $\theta$ . In principle, a single set of  $q$  and  $u$  value is sufficient to determine polarization parameters, but all four stokes parameters are used as a redundancy check. The errors associated with stokes parameters are dominated primarily by photon statistics and is expressed as (Ramaprakash et al. 1998),

$$\sigma_{R(\alpha)} = (\sqrt{N_e + N_o + N_{Be} + N_{Bo}})/(N_e + N_o), \quad (4)$$

which are further propagated appropriately in deriving polarization parameters. Here  $N_o$ ,  $N_e$  are ordinary and extraordinary counts and  $N_{Bo}$ ,  $N_{Be}$  are ordinary and extraordinary background counts respectively for a position  $\alpha$ .

Along with SNe, a number of polarized and unpolarized standards (Schmidt et al. 1992) have been also observed to estimate instrumental polarization and correct the zero-point polarization angle which mainly originate from imperfection in manual alignment of the instrument. For the polarized standards, the degree of polarization  $P$  measured from the instrument is found consistent within limit of errors and any offset found in the measured and standard values of polarization angle  $\theta$  is corrected in the measurements for SNe. Using unpolarized standards, the instrumental polarization is found to vary within 0.03 to 0.10%, which is consistent to that found by other authors for AIMPOL (see e.g., Rautela et al. 2004; Eswaraiyah et al. 2013). Since the direction of polarization is not confined to any particular plane and the value itself is very small (within error limits), we have not subtracted this from our observational measurements.

To get an estimate of the polarization towards the direction of SNe 2013hj and 2014G due to Galactic dust, we also observed a number of bright field stars (on April 22 2015) within an average radius of  $\sim 5^\circ$  around corresponding targets. The  $V$ -band polarization observations of these bright field stars are also presented in Heiles (2000). We have observed 11 and 3 field stars in the direction of SNe 2013hj and 2014G respectively.

The observed polarization measurements for SNe 2013hj and 2014G are listed in Table B1 and those for field stars are tabulated in Table B2.

### 3 DISTANCE AND EXTINCTION

Distance and total line-of-sight extinction are the two parameters which are important to study the intrinsic properties of SNe. Thus it is essential to determine these parameters for each of the SNe, before we characterize and analyze them.

#### SN 2013hj

MCG -02-24-3 hosts SN 2013hj at the edge of the projected view of the diffused spiral galaxy. As there is no redshift independent distance available in the literature, we adopt a redshift distance of  $28.2 \pm 2.0$  Mpc from Hyper1eda<sup>2</sup> (Makarov et al. 2014) corrected for Virgo infall velocity and assuming  $H_0 = 70$  km s<sup>-1</sup>Mpc<sup>-1</sup>,  $\Omega_m = 0.27$ ,  $\Omega_\Lambda = 0.73$ . However there are well accepted techniques which utilizes observations of type II SN itself to determine its distance. EPM (Kirshner & Kwan 1974; Jones et al. 2009; Bose & Kumar 2014) and SCM (Hamuy & Pinto 2002; Olivares et al. 2010) are two such methods which have been successfully implemented on several SNe II to estimate redshift independent distances, but requires extensive spectroscopic information as well which restricts us from implementing these methods on both of these SNe.

The most widely adopted method to estimate line-of-sight extinction is from correlation of narrow Na I D absorption line equivalent width with the reddening  $E(B - V)$  (see Barbon et al. 1990; Turatto et al. 2003; Poznanski et al. 2012). Since our dataset is only limited to photometry, we can not adopt this method which requires SN spectrum of good resolution and high SNR. In order to determine total extinction we need estimates for both Milky way and host galaxy extinction. Using the all-sky Galactic extinction map by Schlafly & Finkbeiner (2011), we adopt a reddening value of  $E(B - V)_{MW} = 0.045 \pm 0.002$  mag due to Milky Way. To have an estimate of extinction due to host galaxy we implement the ‘‘color-method’’ (Olivares et al. 2010), which assumes that intrinsic  $(V - I)$  color towards the plateau end is constant. Olivares et al. (2010) found an empirical relation between color and visual extinction as,

$$\begin{aligned} A_V(V - I) &= 2.518[(V - I) - 0.656] \\ \sigma_{(A_V)} &= 2.518\sqrt{\sigma_{(V-I)}^2 + 0.053^2 + 0.059^2} \end{aligned} \quad (5)$$

Putting a  $(V - I)$  color of  $0.725 \pm 0.031$  mag, which is a low-order cubic interpolated value at 75d and corrected for Galactic extinction, we derive the host galaxy visual extinction of  $A_{V_{host}} = 0.172 \pm 0.069$  mag. Therefore, the adopted total line-of-sight visual extinction is  $A_V = 0.312 \pm 0.214$  mag, which translates to  $E(B - V) = 0.100 \pm 0.069$  mag assuming the ratio of total to selective extinction  $R_V = 3.1$ .

#### SN 2014G

SN 2014G is hosted in the galaxy NGC 3448. From previous studies, only a single redshift independent distance estimate is available using Tully-Fisher method (Tully & Fisher

<sup>2</sup> <http://leda.univ-lyon1.fr/>

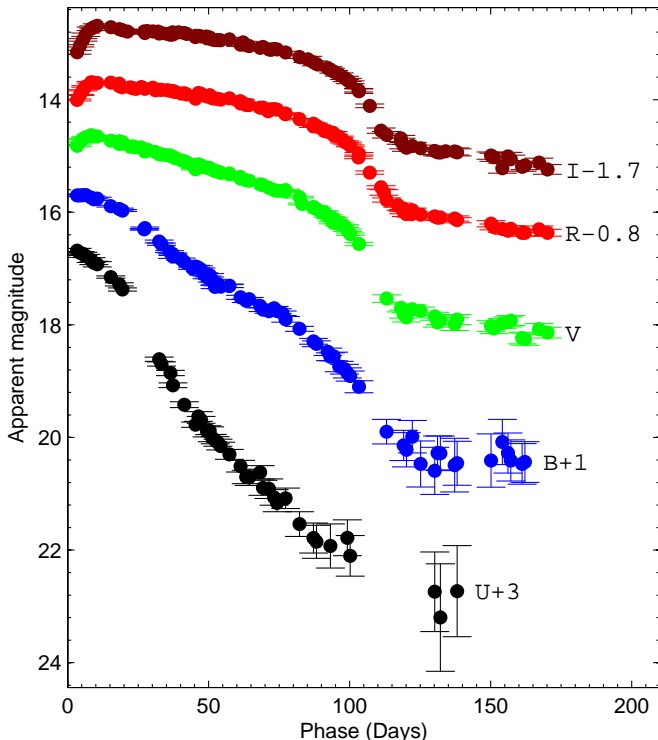


**Figure 3.** The photometric light curve of SN 2013hj in Johnson-Cousins *UBVR I* bands. The light curves are shifted for clarity as indicated on the plot.

1988) for the galaxy, which is  $24.4 \pm 9.0$  Mpc. We adopt this distance for SN 2014G throughout the paper.

The value of reddening due to Milky Way towards NGC 3448 is found to be  $E(B-V)_{\text{MW}} = 0.010 \pm 0.000$  mag from the all-sky Galactic dust-extinction survey (Schlafly & Finkbeiner 2011). To estimate the host galaxy extinction for SN 2014G, we implement the color-method (Olivares et al. 2010) as described in the case of SN 2013hj. Following their prescription, using  $(V-I) = 0.956 \pm 0.038$  mag (interpolated at 56 day after correcting for Galactic extinction) in Eq. 5, we obtain host visual extinction  $A_{V_{\text{host}}} = 0.755 \pm 0.222$  mag. Thus summing up, we adopt a total extinction of  $A_V = 0.787 \pm 0.222$  mag, corresponding to a reddening value  $E(B-V) = 0.254 \pm 0.072$  mag.

## 4 OPTICAL LIGHT CURVE

### 4.1 Apparent magnitude light curves

#### *SN 2013hj*

*UBVR I* broadband photometric observations of SN 2013hj are available at 117 phases from 3 to 170d. The data coverage is dense and almost continuous during this span. The resultant light curves are shown in Fig. 3.

The early light curves show a sharp rise in *RI* bands, which is also visible in *BV* bands but relatively much flatter. After the initial peak the light curves decline slowly until the plateau ends. SN 2013hj does not show very sharp transition in slope at the end of plateau as is seen in generic

SNe IIP, e.g., SNe 1999em (Leonard et al. 2002b), 1999gi (Leonard et al. 2002a), 2004et (Sahu et al. 2006), 2013ab (Bose et al. 2015a). Rather the light curve shows linearity only up to  $\sim 80$ d, thereafter it shows a gradual increase in slope until it reaches the end of plateau at around  $\sim 96 - 100$ d. At the end of plateau, the light curve declines steeply to settle onto a relatively slow declining radioactive tail at  $\sim 118$ d, which continues till the end of our observations.

The light curve parameters of SN 2013hj are listed in Table 2 (Rows:1-3). The time of peak in early light curves (Tab. 2, Row:1) are consistent with most typical and common fast-rising SNe IIP like 2005cs (Pastorello et al. 2009), 2004et (Sahu et al. 2006) and 2013ab (Bose et al. 2015a), which is significantly faster than slow-rising SNe, e.g. SNe 2006bp (Quimby et al. 2007), 2009bw (Inserra et al. 2012) and 2012aw (Bose et al. 2013). After the initial peak the light curves continue to decline during the entire plateau phase, however in *R* and *I* bands a break in slope is visible at 23 and 24 days respectively. This break is possibly the mark of the emergence of recombination phase, as the shock heated ejecta is cooling down and recombination starts to power the light curve. Such a feature, but more prominent, was also seen in *VRI* bands of type IIP SN 2012aw (Bose et al. 2013).

Since the initial peak SN 2013hj continues to decline, but does not show a constant slope towards the plateau end. During 80 to 100d a gradual increase in light curve slope can be seen. The plateau slope for the linear part is listed in Tab. 2 (Row:2). This is steeper than the values reported for generic type IIP SNe 1999em (Leonard et al. 2002b), 1999em (Leonard et al. 2002a), 2012aw (Bose et al. 2013) and 2013ab (Bose et al. 2015a), but flatter than the fast declining SNe like SN 2013by (Valenti et al. 2015), SN 2013ej (Bose et al. 2015b) and 2014G (this paper). For example, decline rates for SN 2012aw are 5.60, 1.74, 0.55 mag  $(100 \text{ d})^{-1}$  in *UBV*-bands and for SN 2013ab decline rates are 7.60, 2.72, 0.92, 0.59 and 0.30 mag  $(100 \text{ d})^{-1}$  in *UBVR I* bands, whereas SN 2013ej decline rates are 6.60, 3.57, 1.74, 1.07 and 0.74 mag  $(100 \text{ d})^{-1}$ . Decline rates for radioactive tail phase in *VRI* bands are listed in Tab. 2 (Row:3), where *U* and *B* band slopes were not computed due to large errors in tail data points.

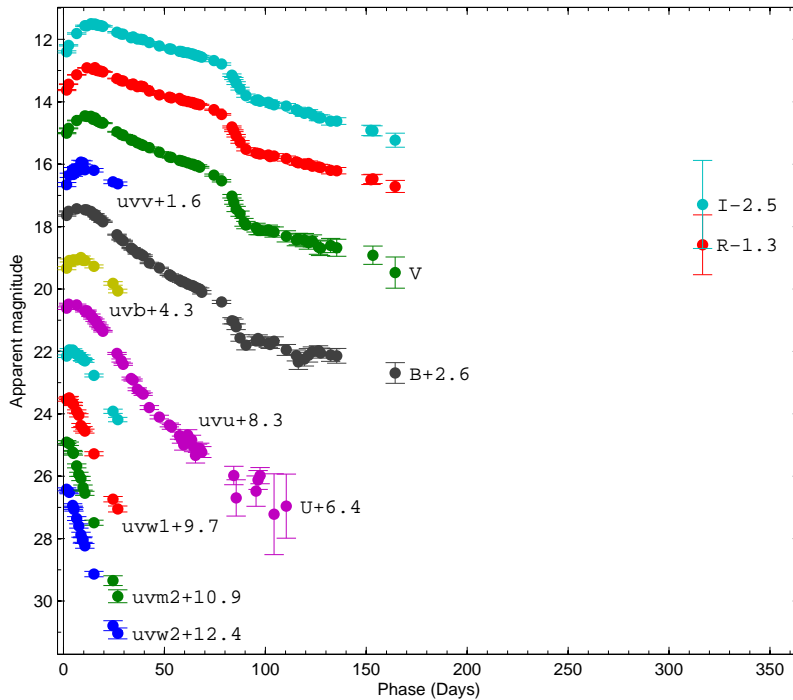
#### *SN 2014G*

Photometric measurements in *UBVR I* bands for SN 2014G were made at 63 phases during 4 to 319d, where continuous and high-cadence observation were only during 4 to 166d, with a late nebular data point at 319d recovered only after galaxy background subtraction. Additionally 15 phases of UVOT observations during 2 to 27d is also available in all six UVOT bands (*uvw1*, *uvw2*, *uvm2*, *uvw*, *uvb* and *uvw*). The light curves are shown in Fig. 4.

The early part of light curves show a sharp rise in most of the optical bands (*BVRI* and *uvb*, *uvw*). The rising is detectable in UV bands as well except for *uvm2* and *uvw2* bands. After the initial peak all the light curves decline linearly until plateau end ( $\sim 77$ d), like a generic SNe IIL (SN 1980K; Barbon et al. 1982 and SN 2013by; Valenti et al. 2015). From  $\sim 77$ d, the light curve decline steeply to en-

**Table 2.** Light curve parameters of SN 2013hj and SN 2014G.

Row No.	Parameter	<i>U</i>	<i>B</i>	<i>V</i>	<i>R</i>	<i>I</i>	<i>uvw2</i>	<i>uvm2</i>	<i>uvw1</i>	<i>uvu</i>	<i>uvb</i>	<i>uvv</i>	
SN 2013hj	1	Rise time of early peak (days)	–	6	8	11	12	–	–	–	–	–	
	2	Plateau slope [mag (100 d) <sup>-1</sup> ]	5.81	3.38	1.50	0.89	0.77	–	–	–	–	–	
	3	Nebular slope [mag (100 d) <sup>-1</sup> ]	–	–	0.72	0.81	0.76	–	–	–	–	–	
SN 2014G	4	Rise time of early peak (days)	6	10	13	15	17	–	–	5	6	10	
	5	Plateau slope [mag (100 d) <sup>-1</sup> ]	6.66	4.09	2.55	1.97	1.83	18.63	20.40	15.33	–	–	–
	6	Nebular slope [mag (100 d) <sup>-1</sup> ]	–	1.40	1.57	1.52	1.78	–	–	–	–	–	

**Figure 4.** The photometric light curve of SN 2014G in Johnson-Cousins *UBVRi* and *Swift* *UVOT* bands. The light curves are shifted for clarity as indicated on the plot.

ter relatively slow declining radioactive tail phase starting from  $\sim 90$ d.

The light curve parameters for SN 2014G are tabulated in Table 2 (Rows:4–6). Early rising of SN 2014G light curve (Tab. 2, Rows:4) is consistent with slow rising SNe, e.g. the *V*-band maximum is delayed to 16d in SN 2006bp (Quimby et al. 2007), 13d in SN 2009bw (Inserra et al. 2012) and 15d in SN 2012aw (Bose et al. 2013). This is significantly slower than most typical type II SNe, like SNe 2005cs, 2004et, 2013ab or the other SN which we present here - SN 2013hj.

After reaching maxima, SN 2014G light curves in all bands shows linear decline throughout the plateau and their decline rates are listed in Tab. 2 (Rows:5). These values are similar to that of type IIL SNe like SN 1980K and SN 2013by, but much steeper than all type IIP SNe (decline rates as mentioned above for SNe 2012aw and 2013ab). For exam-

ple, SN 2013by (Valenti et al. 2015) shows a recline rate of 3.62, 2.01, 1.42 and 1.26 mag (100 d)<sup>-1</sup> in *BVri* bands and 19.53, 20.54 and 15.26 mag (100 d)<sup>-1</sup> in *uvw2*, *uvm2*, *uvw1* bands. The decline rates for radioactive tail light curves are also listed Tab. 2 (Rows:6). The slope of radioactive tail light curve is also found to be steeper than normal IIP SNe (e.g. SN 2013ab tail slopes are 0.36, 0.97, 0.66, 1.16 mag (100 d)<sup>-1</sup> in *BVri* or in SN 2012aw tail slopes are 0.88, 0.88, 0.81, 0.95 mag (100 d)<sup>-1</sup> in *BVRI*) but very similar to that found in SN 2013ej (Bose et al. 2015b, tail slopes are 1.22, 1.53, 1.42, 1.55 mag (100 d)<sup>-1</sup> in *BVRI* bands).

## 4.2 Absolute magnitude light curves

Absolute *V*-band ( $M_V$ ) light curves of SNe 2013hj and 2014G are shown in Fig. 5 and are compared with a moderately sized sample of SNe II. In order to determine light

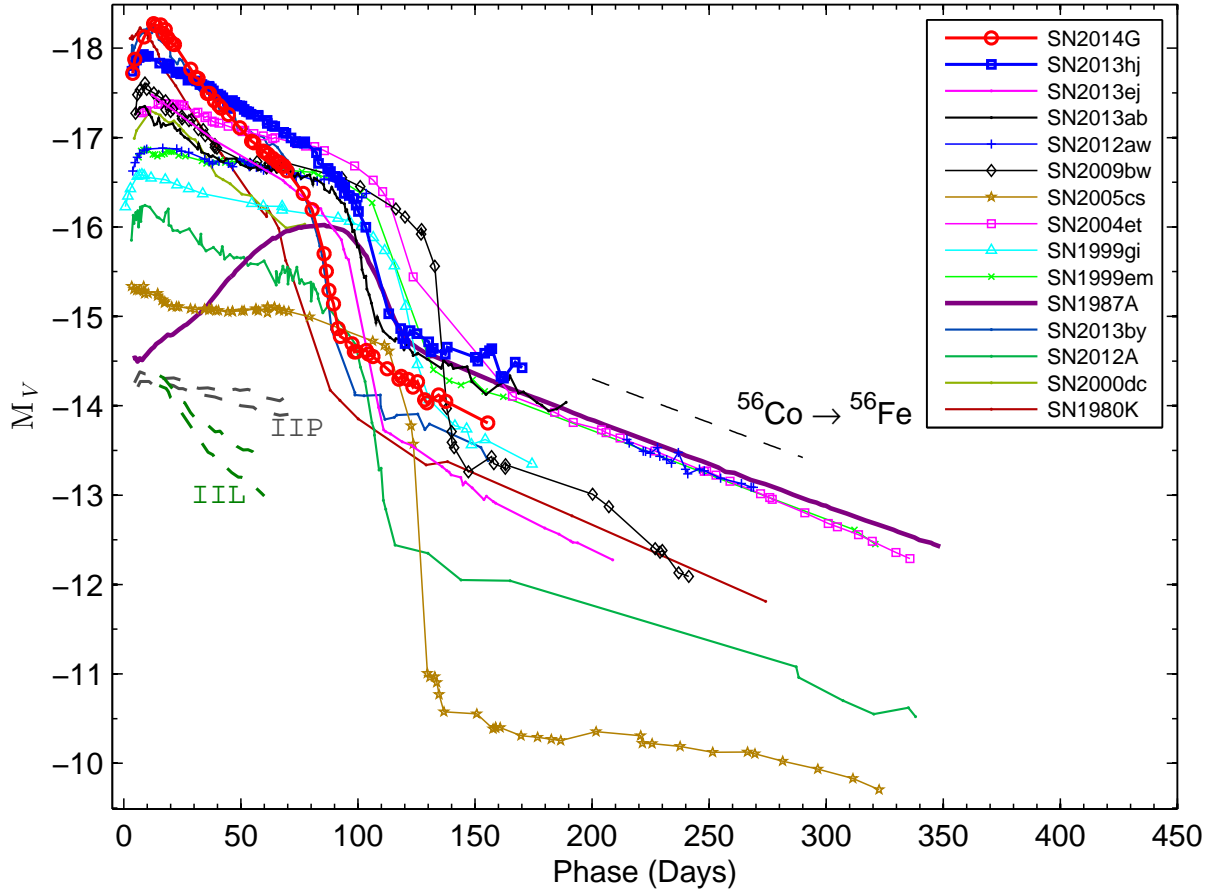


**Figure 5.** Absolute  $V$  band light curves of SNe 2013hj and 2014G are compared with other type II SNe. The exponential decline of the tail light curve following the radioactive decay of  $^{56}\text{Co} \rightarrow ^{56}\text{Fe}$  is shown with a dashed line. On the bottom left side, two pair of dotted lines in gray and green colors represent the slope range for type IIP and IIL SNe templates as presented by [Faran et al. \(2014\)](#). The adopted JD, distance,  $E(B - V)$  and reference for  $V$ -band magnitude are listed in Table 3.

**Table 3.** Adopted parameters and references for  $V$ -band magnitudes for the SNe II sample used in this paper.

SNe	JD 2400000+	Distance (Mpc)	$E(B - V)$ (mag)	Reference for data
SN 1980K	44540.5	5.5	0.30	<a href="#">Barbon et al. (1982)</a> ; NED database <sup>a</sup>
SN 1987A	46849.8	0.05	0.16	<a href="#">Hamuy &amp; Suntzeff (1990)</a>
SN 1999em	51475.6	11.7	0.10	<a href="#">Leonard et al. (2002b)</a> ; <a href="#">Elmhamdi et al. (2003)</a>
SN 1999gi	51522.3	13.0	0.21	<a href="#">Leonard et al. (2002a)</a>
SN 2000dc	51762.4	49.0	0.07	<a href="#">Faran et al. (2014)</a> ; NED database <sup>a</sup>
SN 2004et	53270.5	5.4	0.41	<a href="#">Sahu et al. (2006)</a>
SN 2005cs	53549.0	7.8	0.11	<a href="#">Pastorello et al. (2009)</a>
SN 2009bw	54916.5	20.2	0.31	<a href="#">Inserra et al. (2012)</a>
SN 2012A	55933.5	9.8	0.04	<a href="#">Tomasella et al. (2013)</a>
SN 2012aw	56002.6	9.9	0.07	<a href="#">Bose et al. (2013)</a>
SN 2013ab	56340.0	24.0	0.04	<a href="#">Bose et al. (2015a)</a>
SN 2013by	56404.0	14.8	0.19	<a href="#">Valenti et al. (2015)</a>
SN 2013ej	56497.3	9.6	0.06	<a href="#">Bose et al. (2015b)</a>

<sup>a</sup> <http://ned.ipac.caltech.edu>

**Table 4.** Parameters estimated from V band light curve

SN Name	Plateau slope <sup>a</sup> mag (100 d) <sup>-1</sup>	Transition drop <sup>b</sup> mag	Transition time <sup>c</sup> days
SN1980K	3.63 ± 0.04	2.0±0.2	37 ± 5
SN2000dc	2.56 ± 0.06 <sup>i</sup>	–	–
SN2014G	2.55 ± 0.02	1.6±0.2	17 ± 2
SN2013by	2.01 ± 0.02	2.2±0.2	19 ± 5
SN2013ej	1.74 ± 0.08	2.4±0.1	21 ± 3
SN2013hj	1.50 ± 0.02	1.5±0.2	22 ± 5
SN2012A	1.12 ± 0.03	2.5±0.1	23 ± 4
SN2009bw	0.93 ± 0.04	2.4±0.2	14 ± 3
SN2004et	0.73 ± 0.02	2.1±0.2	27 ± 6
SN2013ab	0.54 ± 0.02	1.7±0.1	25 ± 2
SN2012aw	0.51 ± 0.02	–	–
SN1999gi	0.47 ± 0.02	2.0±0.1	29 ± 3
SN2005cs	0.44 ± 0.03	4.0±0.1	24 ± 3
SN1999em	0.31 ± 0.02	1.9±0.1	28 ± 4

Note: Objects are sorted in order of descending plateau slope.

<sup>a</sup> Plateau slope during the linear decline phase, starting after first minima until plateau end.

<sup>b</sup> Drop in magnitude during the plateau to nebular transition.

<sup>c</sup> Duration of plateau to nebular transition.

<sup>i</sup> Slope is calculated up to the available range of data, as plateau end is not observed.

curve characteristics of these two SNe and mark their position in the type II diversity, we selected the comparison sample with diverse range of properties, comprising of archetypal type IIP SNe 1999em, 1999gi, 2012aw to prototypical type IIL SN 1980K. The plateau slopes for all SNe II sample shown in Fig. 5 are listed in Table. 4. This table and figure is primarily an adaptation from Bose et al. (2015b).

The mid plateau absolute magnitude for SN 2013hj is highest amongst the compared sample of events. However, it may be noted that the uncertainty in adopted reddening and distance values may alter this inference to some extent. The plateau decline rate of SN 2013hj is higher than most generic IIP SNe (e.g., SN 1999em, SN 2005cs, SN 2012aw) but lower than IIL SNe 1980K or 2000dc. According to Faran et al. (2014), type II SN with plateau decline of at least 0.5 mag in first 50 days would be classified as type IIL, which would definitely classify SN 2013hj as type IIL. However, this criteria proposed by Faran et al. (2014) is a bit too rigid, as it would reclassify all SNe up to slopes of SN 2012A (see Table 4) as type IIL. Faran et al. (2014) also presented template light curve range for SNe IIP and IIL, which is shown in Fig. 5. The plateau slope for SN 2013hj is marginally smaller than the minimum slope for the SNe IIL templates but it is much larger than the steepest slope for the SNe IIP templates. Thus, if SN 2013hj has to be classified either between type IIP or IIL, it would fit best in the class of type IIL rather than type IIP. The closest comparison to SN 2013hj in terms of plateau slope, shape and duration is SN 2013ej. However, plateau decline of SN 2013ej is a bit more steep than SN 2013hj making it compatible to SNe IIL light curve templates.

On the other hand, owing to the fast decline of SN 2014G, its mid-plateau magnitude is lower than SN 2013hj, but the peak luminosity is highest amongst the compared sample. The decline rate is higher than all SNe II in the

sample, except for prototypical type IIL SN 1980K and SN 2000dc. The plateau slope of SN 2014G is marginally over the SNe IIL template, thus clearly qualifying as a type IIL SN. SN 2013by is the closest comparison to SN 2014G in terms of light curve shape and magnitudes except for the fact that SN 2014G plateau is steeper and the nebular tail is brighter. The decline rate of tail light curve is 1.57 mag (100 d)<sup>-1</sup>, which is higher than that expected for light curve powered from radioactive decay of <sup>56</sup>Co to <sup>56</sup>Fe. However, such steepening of tail light curve was also seen in other type IIL SNe as well. For example, SN 2013ej exhibits a steeper decline rate of 1.53 mag (100 d)<sup>-1</sup> (Bose et al. 2015b), similarly other IIL SNe 1980K and 2013by also show steeper declines like SN 2014G (see Fig. 5). In Fig. 6 we show the *Swift* UVOT absolute magnitude light curves for SN 2014G in UV bands and are compared with other SNe II which are well observed by UVOT. UV light curve evolution of SN 2014G is found similar to other SNe. The peak brightness closely matches to that of SN 2013by but is higher than most other SNe in the sample.

Based on the light curve parameters, SN 2014G is a perfect example of a generic type IIL SN whereas SN 2013hj belongs to an intermediate class with plateau slope close but lower than typical SNe IIL. With the adopted reddening and distance values, both the SNe lie on the luminous end of the comparison sample, which may eventually fall in the range of normal luminosity if reddening or distance values are lowered. Anderson et al. (2014) found an anti-correlation between the plateau slope and duration, which is consistent with the trend as we see for SNe 2013hj and 2014G as well as other SNe in the sample.

### 4.3 Bolometric light curve

Pseudo-bolometric light curves for SNe 2013hj and 2014G are computed using photometric fluxes corrected for adopted reddening and distance values. We follow the same method as outlined in Bose et al. (2013) to compute bolometric luminosities, which involves semi-deconvolution of broadband filter response from photometric fluxes. Thermal emission from SNe mostly peaks in optical and near-optical wavelengths depending on the phase of SN evolution. At early phases (< 30d) when the SN is hot, UV wavelengths dominate bolometric luminosity. Likewise, at late phases (> 100d) when the SN is cool enough, bolometric light is dominated by infrared fluxes. We compute pseudo-bolometric luminosity for both the SNe in the optical domain, which include *UBVRI* fluxes. For SN 2014G we also computed bolometric luminosity by taking UV fluxes into account, which include fluxes from *uvw2* to I bands. The UV+Optical luminosity yields a significantly higher value at early times. In Fig. 7 we compare bolometric light curves of SNe 2013hj and 2014G with other well-studied SNe. The bolometric light curves of the comparison sample were also computed using the same method and within the same wavelength range.

Bolometric light of SN 2013hj suffers almost a linear decline during 6 to 100d with a luminosity drop of ~ 0.85 dex. This decline rate is similar to SN 2013ej, but higher than most generic IIP SNe in the sample. An additional drop of 0.47 dex is seen at the end of plateau while light curve settles onto the radioactive nebular tail phase since 118d. The slope of tail light curve is similar to those of SNe

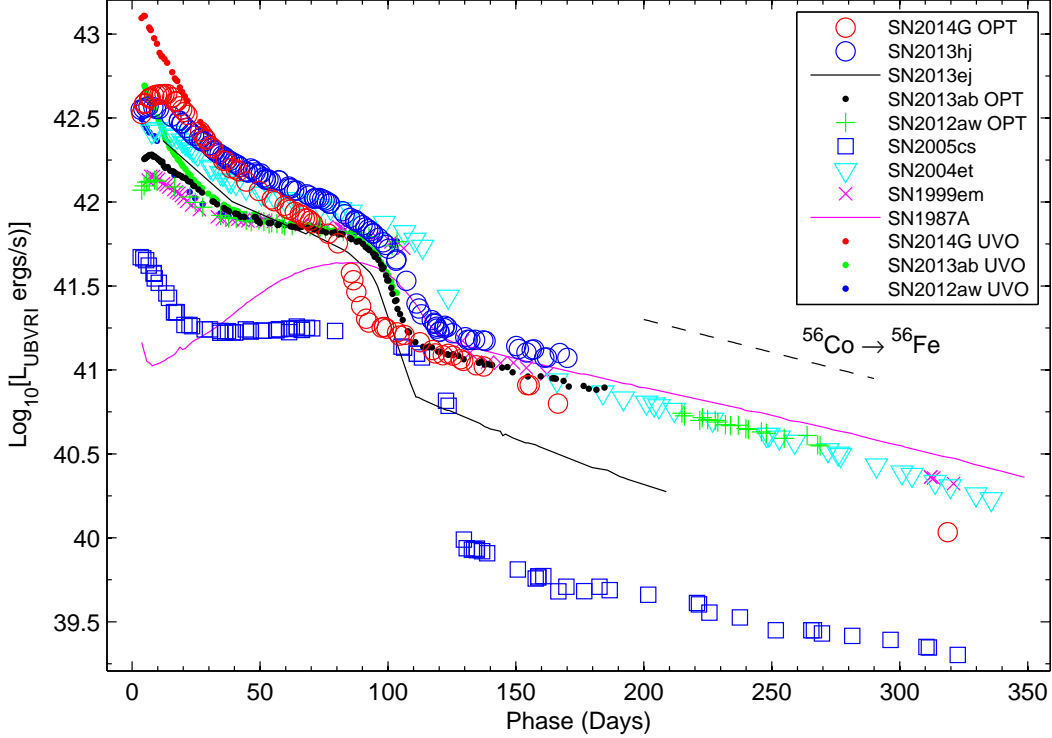


**Figure 7.** The  $UBVRI$  pseudo-bolometric light curves of SNe 2013hj and 2014G are compared with those of other well studied SNe. Light curves with added *Swift* UVOT UV contributions are also shown for SN 2013ej, SN 2013ab and SN 2012aw (labeled as UVO). The adopted distances, reddening and time of explosion values are listed in Table 3. The exponential decline of the radioactive  $^{56}\text{Co}$  decay law is shown with a dashed line.

1987A, 1999em, 2004et and 2013ab which is consistent to that expected for  $^{56}\text{Co}$  to  $^{56}\text{Fe}$  radioactive decay rate.

SN 2014G shows a decline rate higher than all compared SNe including SN 2013hj. SN 2014G shows a linear decline throughout the plateau phase and experiences a drop of 0.89 dex in bolometric luminosity during 13 to 80d. A drop of 0.49 dex in luminosity is seen during the transition from plateau to nebular phase. SN 2014G light curve settles onto relatively slow declining radioactive tail phase after 92d. The slope during this phase is found to be somewhat steeper ( $0.39 \text{ dex } (100)^{-1}\text{d}$ ) than other generic IIP SNe (e.g. SNe 1987A, 1999em, 2004et, 2013ab), and also that expected for a light curve powered by radioactive decay of  $^{56}\text{Co}$  to  $^{56}\text{Fe}$ . On careful examination of the absolute  $V$ -band and bolometric light curve (see Figs. 5 and 7), such steepening of tail light curve is also seen in other type IIL SNe 1980K, 2013by and 2013ej. Steepening of tail light curve would indicate inefficient trapping of gamma rays in the ejecta. In type IIL SNe, the hydrogen envelope is relatively more depleted than IIP counterpart, resulting into lower gamma ray optical depth causing leakage of gamma photons. Such a scenario may explain steeper tail light curve in SN 2014G, and this may also be true for all other fast declining SNe IIL as well. However, due to fast decaying brightness, there are only a handful of SNe IIL with observations extending up to the tail phase and SN 2014G is the newest among such candidates.

#### 4.4 Mass of nickel

In CCSNe, radioactive  $^{56}\text{Ni}$  is produced by explosive nucleosynthesis at the time of explosion. The nebular phase light curve is mainly powered by the radioactive decay chain of  $^{56}\text{Ni}$  to  $^{56}\text{Co}$  and  $^{56}\text{Co}$  to  $^{56}\text{Fe}$ , with  $e$ -folding life time of 8.8 and 111.26 d respectively. Thus, the tail luminosity would be proportional to the amount of radioactive nickel synthesized at the time of explosion.

SN 1987A is one of the most well studied SN with a fair degree of accuracy in the estimation of  $^{56}\text{Ni}$  mass ( $0.075 \pm 0.005 M_{\odot}$ ; Arnett 1980). By comparing the tail luminosity of a SN with that of SN 1987A, we can estimate the mass of  $^{56}\text{Ni}$  for that SN as well. Although in principle true bolometric luminosities (including UV, optical and IR) are to be used to compute  $^{56}\text{Ni}$  mass, but we do not have IR fluxes for either of SN 2013hj or SN 2014G. For the uniformity in comparison we also use  $UBVRI$  bolometric luminosity for SN 1987A, computed using the same method and wavelength range. We compute the ratio of SN 2013hj to SN 1987A luminosity at 150d to be  $1.152 \pm 0.168$ . This corresponds to a  $^{56}\text{Ni}$  mass of  $M_{\text{Ni}}(2013\text{hj}) = 0.086 \pm 0.013 M_{\odot}$ . Similarly, the ratio of SN 2014G to SN 1987A luminosity at 150d is  $0.735 \pm 0.552$ , which corresponds to  $M_{\text{Ni}}(2014\text{G}) = 0.055 \pm 0.041 M_{\odot}$ .

The gamma photons emitted from the radioactive decay of  $^{56}\text{Co}$  to  $^{56}\text{Fe}$  are assumed to thermalize the ejecta powering the tail light curve, which in turn depends on the initial mass of synthesized  $^{56}\text{Ni}$ . Hamuy (2003) related these

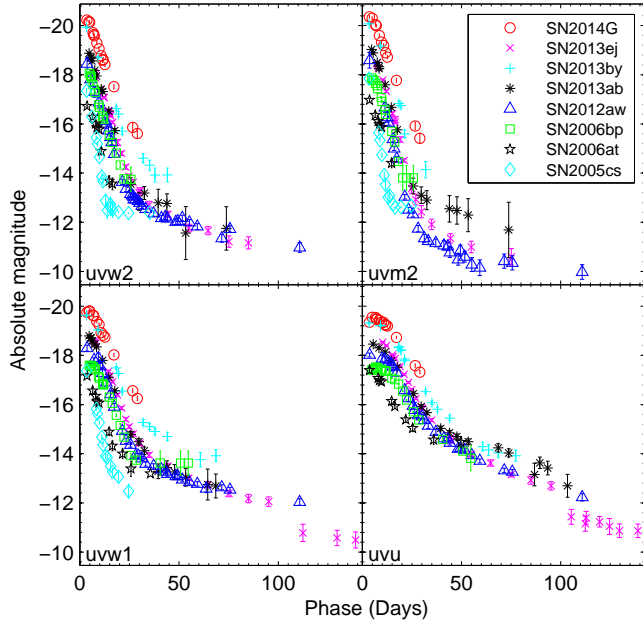


**Figure 6.** *Swift* UVOT UV absolute light curves of SN 2014G is compared with other well observed SNe II from UVOT. For the compared SNe, references for UVOT data, extinction and distance are: SN 2005cs – Brown et al. (2009); Pastorello et al. (2009), SN 2006at – Brown et al. (2009); Distance 65 Mpc;  $E(B - V) = 0.031$  mag (only Galactic reddening Schlafly & Finkbeiner 2011), SN 2006bp – Dessart et al. (2008), SN 2012aw – Bayless et al. (2013); Bose et al. (2013), SN 2013by – Valenti et al. (2015), SN 2013ej – (Bose et al. 2015b).

parameters as,

$$M_{\text{Ni}} = 7.866 \times 10^{-44} \times L_t \exp \left[ \frac{(t_t - t_0)/(1+z) - 6.1}{111.26} \right] M_{\odot},$$

where  $t_0$  is the explosion time, 6.1d is the half-life of  $^{56}\text{Ni}$  and 111.26d is the e-folding time of the  $^{56}\text{Co}$  decay. Using the bolometric correction factor for tail phase as given by Hamuy (2003), we compute a tail luminosity of  $2.71 \pm 0.20 \times 10^{41}$  erg at 150d for SN 2013hj, which correspond to  $^{56}\text{Ni}$  mass of  $M_{\text{Ni}}(2013\text{hj}) = 0.077 \pm 0.010 M_{\odot}$ . Likewise, tail luminosity of SN 2014G at 140d is  $1.78 \pm 1.01 \times 10^{41}$  erg corresponding to  $M_{\text{Ni}}(2014\text{G}) = 0.045 \pm 0.035 M_{\odot}$ .

The amount of  $^{56}\text{Ni}$  masses estimated from both the methods are consistent with each other within errors. Thus we adopt a mean value of both the results, which is  $M_{\text{Ni}}(2013\text{hj}) = 0.080 \pm 0.008 M_{\odot}$  for SN 2013hj, and  $M_{\text{Ni}}(2014\text{G}) = 0.050 \pm 0.027 M_{\odot}$  for SN 2014G. Although the quoted errors in  $^{56}\text{Ni}$  mass include uncertainty from adopted reddening and distance values, but does not take care of selection bias involved in these parameters. Estimated  $^{56}\text{Ni}$  masses may be lowered if lower values of reddening or distance is assumed.

## 5 LIGHT CURVE MODELLING

We model the bolometric light curves of SNe 2013hj and 2014G following the semi-analytical approach origi-

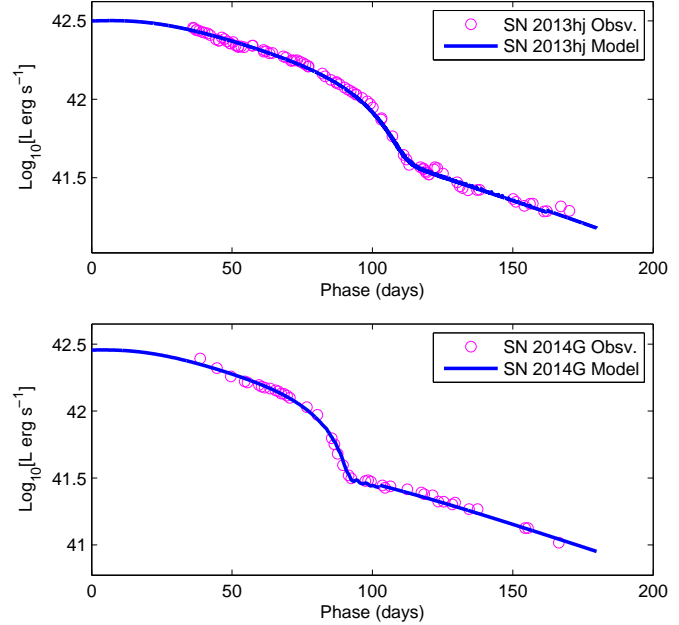


**Figure 8.** The observed bolometric light curves of SNe 2013hj and 2014G are shown with the best fit model.

nally developed by Arnett (1980) and further refined in Arnett & Fu (1989). Such simplistic models (e.g. Arnett 1980, 1982; Arnett & Fu 1989; Popov 1993; Zampieri et al. 2003; Chatzopoulos et al. 2012) are useful to get a preliminary yet reliable estimate of explosion parameters without running more accurate but resource intensive hydrodynamical models (e.g. Falk & Arnett 1977; Utrobin 2007; Bersten et al. 2011; Pumo & Zampieri 2011). The model has been implemented by Nagy et al. (2014) and Bose et al. (2015b) for several type II SNe to estimate explosion parameters and are found to be fairly consistent with results from hydrodynamical models.

Description of model formulation and algorithm is presented in Bose et al. (2015b) and references therein. The temporal component of temperature evolution in a co-moving frame of expansion is given (Arnett & Fu 1989; Nagy et al. 2014) as,

$$\frac{d\phi(t)}{dz} = \frac{R(t)}{R_0 x_i^3} \left[ p_1 \zeta(t) - p_2 \phi(t) x_i - 2x_i^2 \phi(t) \frac{R_0}{R(t)} \frac{dx_i}{dz} \right], \quad (6)$$

which is numerically solved with appropriate treatment of dimensionless recombination front  $x_i$ . After finding the solution for  $\phi(t)$  and  $x_i$ , the model luminosity is computed as (Arnett & Fu 1989; Nagy et al. 2014; Bose et al. 2015b),

$$L(t) = x_i \frac{\phi(t) E_{th}(0)}{\tau_d} \left( 1 - e^{-A_g/t^2} \right) + 4\pi r_i^2 Q \rho(x_i, t) R(t) \frac{dx_i}{dt}. \quad (7)$$

The parameters in these equations have standard meaning as referred in aforementioned papers.  $A_g$  is the effectiveness of gamma ray trapping (see e.g., Clocciatti & Wheeler 1997; Chatzopoulos et al. 2012) which is an important parameter to model a radioactive tail steeper than that expected for light curve powered by decay chain of  $^{56}\text{Ni} \rightarrow ^{56}\text{Co} \rightarrow ^{56}\text{Fe}$ .

To implement the model, we require true bolometric luminosities for the SNe. Since our data is limited only to UV and optical, we add IR flux contribution assuming SNe

2013hj and 2014G have similar optical to IR flux ratio as observed for SN 1999em at similar phases. Fig. 8 shows the computed bolometric light curves of SNe 2013hj and 2014G fitted with our model. Since these models are inefficient to reproduce post-breakout peaks of early light curves, we restricted the data only from later part of photospheric phase.

From the best fit model of SN 2013hj we estimate an ejecta mass of  $9.6 M_{\odot}$ , progenitor radius of  $700 R_{\odot}$  and total explosion energy  $\sim 2.1$  foe. The mass of radioactive  $^{56}\text{Ni}$  incorporated in the model is  $0.075 M_{\odot}$ , which is consistent to the value estimated in Section 4.4. Assuming the mass of compact remnant to be  $1.5\text{--}2.0 M_{\odot}$ , the total progenitor mass adds up to  $\sim 11 M_{\odot}$ .

Similarly for SN 2014G, model estimated ejecta mass is  $7.0 M_{\odot}$ , progenitor radius is  $630 R_{\odot}$  and total explosion energy is  $\sim 2.1$  foe.  $^{56}\text{Ni}$  mass determined from model is  $0.052 M_{\odot}$  which is almost equal to the value estimated in Section 4.4. Adding up a mass of  $1.5\text{--}2.0 M_{\odot}$  for the compact remnant, the total progenitor mass is  $\sim 9 M_{\odot}$ . To fit the steeper tail light curve of SN 2014G, as already discussed in Sections 4.1 and 4.3, we increased the gamma ray leakage in the model by lowering the effectiveness of gamma ray trapping parameter  $A_g$  to  $4 \times 10^4 \text{day}^2$ . This parameter is related to gamma-ray optical depth as  $\tau_g \sim A_g/t^2$ .

## 6 BROADBAND POLARIMETRY

Broadband polarimetric observations in  $R$ -band has been carried out for SN 2013hj at 5 phases during 23 to 86d, whereas for SN 2014G only 3 phases of observation during 12 to 25d are available. The observed temporal evolution of  $P$  and  $\theta$  (dashed lines indicate measurement that have not been corrected for any ISP) for both the SNe, along with  $R$ -band absolute light curve is plotted in Fig. 9 (data is tabulated in Table. B1).

### 6.1 Estimation of interstellar polarization

The observed polarization in supernova light primarily has three components, intrinsic polarization due to SN itself, interstellar polarization due to Milk Way ( $\text{ISP}_{\text{MW}}$ ) and interstellar polarization due to host galaxy ( $\text{ISP}_{\text{HG}}$ ). Thus, in order to interpret the intrinsic polarization of SN, we need to subtract ISP components from the observed polarization. However, there is no completely reliable method to derive ISP and thus poses an issue in SN polarimetric studies. Number of methods have been proposed to estimate ISP (Trammell et al. 1993; Tran et al. 1997; Wang et al. 2001), but all involve some assumptions which are not always valid (Wang & Wheeler 2008). Having this limitation, best possible attempt has been made to have a reasonable estimate of ISPs which are discussed in following sections.

#### 6.1.1 Milky way

To get an estimate of  $\text{ISP}_{\text{MW}}$ , we observed 11 bright stars towards the direction of SN 2013hj, within a maximum radius of  $8^\circ$  around the SN. The  $V$ -band polarization measurements of these stars are available in Heiles (2000) catalog. Similarly, field stars have also been observed towards the direction of SN 2014G, but due to scarcity of bright stars

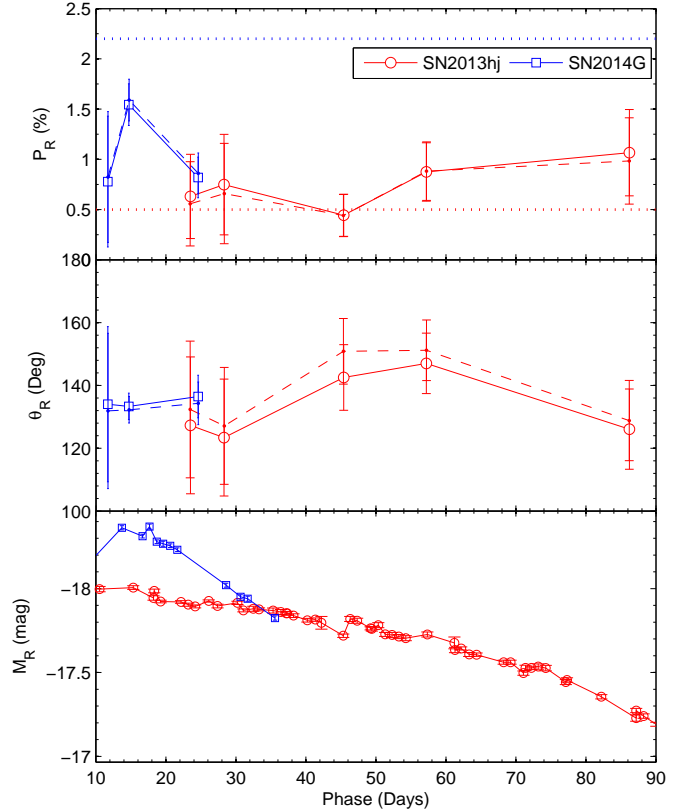


**Figure 9.** The degree of polarization  $P$ , polarization angle  $\theta$  and absolute  $R$ -band magnitude  $M_R$  is plotted in three panels for SNe 2013hj and 2014G. The dashed lines in polarization plots represent the observed polarization parameters, whereas the solid connected plots represent polarization parameters after subtracting for  $\text{ISP}_{\text{MW}}$ . The horizontal dotted lines in top panel represents maximum amount of host galaxy polarization ( $P_{\text{max}} < 9 \times E(B - V)$ ; Serkowski et al. 1975) component that could be present in SN polarization values (0.50 and 2.20 % for SNe 2013hj and 2014G respectively; see Sec. 6.1.2) which may be linearly subtracted if the polarization angles of host and SN are co-aligned.  $R$ -band light curves are truncated to only show phases where polarimetric data exists.

only 3 have been selected (within a maximum radius of  $13^\circ$ ) also having polarization measurements in Heiles (2000). All these selected stars have very low  $V$ -band polarization values listed (Heiles 2000). The measured  $R$ -band polarization (see Table B2) for these stars was also found to be low and of similar order as that of the  $V$ -band. To compute the median ISP from observed stars, averaging is done on stokes components and which is then converted back to polarization parameters. The median of stokes components are computed as,

$$\begin{aligned} \langle Q \rangle &= \langle P_i \cos(2\theta_i) \rangle_{i=1..n} \\ \langle U \rangle &= \langle P_i \sin(2\theta_i) \rangle_{i=1..n} \end{aligned} \quad (8)$$

which are then converted back to polarization parameters,

$$\begin{aligned} P_{\text{MW}} &= \sqrt{\langle Q \rangle^2 + \langle U \rangle^2} \\ \theta_{\text{MW}} &= \frac{1}{2} \tan^{-1} \left( \frac{\langle U \rangle}{\langle Q \rangle} \right). \end{aligned} \quad (9)$$

Thus, we obtain median  $\text{ISP}_{\text{MW}}$  as  $P_{\text{MW}} = 0.13 \pm 0.06\%$  and  $\theta_{\text{MW}} = 12.4 \pm 10.3^\circ$  for SN 2013hj, while for SN 2014G,  $P_{\text{MW}} = 0.08 \pm 0.22\%$  and  $\theta_{\text{MW}} = 106.6 \pm 68.5^\circ$ . These  $\text{ISP}_{\text{MW}}$  values are then vectorially subtracted from the observed SN polarization which are also listed in Table B1 and plotted in (connected solid lines) Fig. 9.

According to Serkowski et al. (1975) the interstellar polarization efficiency due to Galactic dust is highly correlated to line-of-sight reddening, which may vary from 3 to 9 times the reddening value. As a reasonable approximation we adopt the mean polarization efficiency as  $P_{\text{mean}} = 5 \times E(B - V)$ . Using this relation and Galactic reddening values adopted (refer Section 3) towards the direction each SN, we get  $P_{\text{mean}}$  value of  $\sim 0.23\%$  and  $\sim 0.05\%$  for SNe 2013hj and 2014G respectively. These are roughly consistent with the  $\text{ISP}_{\text{MW}}$  values we computed from observations of field stars, which implies that Galactic ISM follows the mean polarization efficiency.

### 6.1.2 Host galaxy

For an accurate estimation of  $\text{ISP}_{\text{HG}}$ , one needs to know dust grain properties and magnetic field orientation along the line of sight within the host galaxy. In context to few SNe studies, it has been found that size of dust grains in respective host galaxy were dissimilar to Galactic dust grains (see e.g. SN 1986G; Hough et al. 1987 and SN 2001el; Wang et al. 2003). Due to very diverse nature of dust grains in various galaxies, it is non trivial to adopt mean polarization efficiency without the knowledge of grain properties. However, in order to get an idea of  $\text{ISP}_{\text{HG}}$  and for the sake of understanding its possible implication in SN polarization measurements, we assume dust grain properties of galaxies MCG -02-24-3 (for SN 2013hj) and NGC 3448 (for SN 2014G) are similar to Galactic dust. Now, we may estimate the maximum degree of polarization due to host galaxies following the Serkowski et al. (1975) relation,  $P_{\text{max}} < 9 \times E(B - V)$ . In Section 3 we estimated host galaxy extinctions for both the SNe using color-method, which translates to  $E(B - V)_{\text{host}}$  values of 0.055 and 0.244 mag for SNe 2013hj and 2014G respectively, assuming  $R_V = 3.1$ . Therefore, the corresponding  $P_{\text{max}}$  (for host) values are  $< 0.50\%$  and  $< 2.20\%$  for SNe 2013hj and 2014G respectively.

To vectorially remove ISP components from SN polarization one need to know the direction information as well. It is generally believed and also found to be true that galactic magnetic fields run along the spiral arms (Scarrott et al. 1990, 1991; Han 2009), which is roughly perpendicular to the line joining galactic center and position of spiral arm (see e.g., Kumar et al. 2014; Leonard et al. 2001; Maund et al. 2007). However, in case of both SNe 2013hj and 2014G the host galaxies are almost irregular, not in face-on projection and SN location is not well resolved, this makes it difficult to make any reasonable estimate of the magnetic field orientation and effective line of sight polarization angle at SN locations.

Despite emphasizing all the critical aspects of  $\text{ISP}_{\text{HG}}$ , we do not subtract it from SN polarization measurements and make any speculative inference based on that. This was done mainly because of three uncertainties, (a) the reddening estimation of host galaxy is quite uncertain and may suffer systematic bias due to the method itself (see Section

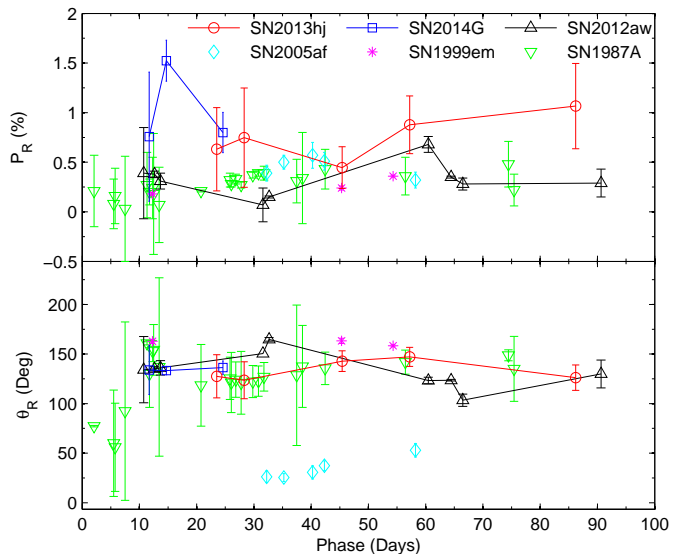


**Figure 10.** Broadband polarimetric evolution of SNe 2013hj and 2014G (only  $\text{ISP}_{\text{MW}}$  subtracted values) are compared with other type IIP SNe. The references for data and explosion epochs are: SN 1987A – Barrett (1988), SN 1999em – Leonard et al. (2001, 2002b), SN 2005af – Pereyra et al. (2006); Filippenko & Foley (2005) and SN 2012aw – Kumar et al. (2014).

3), (b) unknown grain properties in host galaxy may significantly vary the maximum polarization efficiency we are adopting and (c) without knowing the polarization angle of host galaxy vectorial subtraction will not be possible as a subtraction of ISP component may increase or decrease polarization values depending on  $\theta$ . Thus, we caution the reader while interpreting the quoted polarization values as well as Figures 9 and 10 in the paper.

## 6.2 Intrinsic polarization and its evolution

The evolution of degree of polarization and the polarization angle of SNe 2013hj and 2014G are represented in Fig. 9. The evolution of polarimetric parameters of both the events are also compared with other well sampled SNe IIP as shown in Fig. 10. Here SN 1999em observations are  $V$ -band polarimetry, however temporal evolution in  $R$ -band is expected to be similar. In both the figures the polarization values for SNe 2013hj and 2014G are subtracted for  $\text{ISP}_{\text{MW}}$  only, thus these measurements have components for intrinsic SN polarization as well as  $\text{ISP}_{\text{HG}}$ . In Fig. 9 horizontal dotted lines are shown to represent the maximum degree of host polarization component which may be removed if orientation of host and measured SN polarization are assumed to be co-aligned. For any other  $\theta$  of  $\text{ISP}_{\text{HG}}$ , the component of  $P$  due to  $\text{ISP}_{\text{HG}}$  in observed light will be lower than this level and so the intrinsic SN polarization will increase.

It is to be noted in Fig. 9 that there is a small, yet significant amount of intrinsic polarization is left in SN 2013hj even after considering maximum possible subtraction of  $\text{ISP}_{\text{HG}}$ . About  $0.3 - 0.5\%$  of polarization can be detected above maximum  $\text{ISP}_{\text{HG}}$  during 57 and 86d, which is well above the error bars of individual data points. The  $P$  and  $\theta$  evolution does not show a significant relative vari-

ation among individual data points and is all within the limit of errors. However, a subtle increasing trend is noticed in overall  $P$  evolution, but  $\theta$  remains almost constant throughout. This may imply that there is some asymmetry in electron scattering SN envelope, which is increasing according to envelope size and decrease in optical depth is revealing the asymmetric central part of explosion, but its geometrical orientation remains constant over time. It may be noted that the possible increase in polarization with time is almost linearly anti-correlated with the decline of SN brightness. Such monotonic increase in polarization without change in polarization angle has been also observed in SN 1999em (see Fig. 10) which was reported by Leonard et al. (2001); Leonard & Filippenko (2005).

SN 2014G has only three measurements within first 25d. If maximum amount of  $ISP_{HG}$  is considered then entire detection is possibly submerged within the  $ISP_{HG}$  (see Fig. 9). The polarization angle for  $ISP_{HG}$  would play an important role in this case, only after knowing which we may conclude about the intrinsic polarization or asymmetry in SN envelope or CSM. Any favorable misalignment of  $ISP_{HG}$  angle may lead to significant residual SN polarization. A sudden and unusual increase in polarization in noticed at 15d which is coincident with the peak  $R$ -band light, although no change in polarization angle is observed. However, considering the large errors and low density of observations, we restrict ourselves from making any conclusive inference based on a single measurement which may be resulting from a spurious detection.

## 7 SUMMARY

In this paper we present high-cadence photometric observation and a few epochs of broadband polarimetric observation of two fast declining type II SNe 2013hj and 2014G.

Due to lack of reliable handle on distance and reddening estimation, we adopted distance from single Tully fisher measurement or redshift distance available in literature, whereas host galactic reddening is estimate using ‘color-method’ which itself is not very reliable. Details of these methods and adapted values are discussed in Section 3. Implications of these uncertainties on the derived parameters and properties must be considered while making any interpretation. Although the derived parameters include the uncertainty from reddening and distance values, but it does not take care of the possible selection bias which might have been introduced while adopting those values.

The plateau slope of SN 2013hj is significantly steeper ( $1.5 \text{ mag } (100 \text{ d})^{-1}$  in  $V$ ) than typical SNe IIP, but is similar to generic SNe IIL templates (Faran et al. 2014). SN 2013hj is found to lie at an intermediate position in the broad continuum of light curve properties of SNe II diversity (see Anderson et al. 2014). If at all SN 2013hj has to be classified in IIP/L taxonomy, then it will qualify better as a type IIL. SN 2013hj does not show a sharp change in slope at plateau end ( $\sim 98\text{d}$ ) as we see in typical SNe IIP/L, rather a gradual increase of slope is observed. On the other hand, SN 2014G is a perfect IIL candidate showing high initial peak brightness and steep plateau slope ( $2.55 \text{ mag } (100 \text{ d})^{-1}$  in  $V$ ) which lies at the higher end of SNe IIL light curve tem-

plate. A sharp end of plateau phase is visible at  $\sim 77\text{d}$  for SN 2014G.

Owing to fast decline of brightness, most IIL SNe do not have post-plateau observations. SN 2014G is among the very few SNe IIL which has extensive observations covering all the light curve phases until nebular tail. The plateau-nebular transitional drop in luminosity is also prominent for the SN which is although expected but rarely detected for SNe IIL (Anderson et al. 2014). Radioactive tail of SN 2014G is found to be steeper than that expected for a light curve powered by radioactive decay chain of  $^{56}\text{Ni} \rightarrow ^{56}\text{Co} \rightarrow ^{56}\text{Fe}$ . Such steepening is explained by inefficient trapping of gamma rays in the ejecta. The tail light curves of type IIL SNe 1980K, 2013by and 2013ej also shows a significant steepening. This possibly implies that all type IIL SNe may exhibit such steepening of tail light curve, as SNe IIL has thinner hydrogen envelope which is responsible for gamma ray leakage and incomplete thermalization of photons. More type IIL SNe are needed to be observed rigorously until nebular phase to confirm whether steepening of tail is generic feature to all SNe IIL. The mass of synthesized radioactive  $^{56}\text{Ni}$  estimated from tail bolometric light curves are  $0.08 \pm 0.01M_{\odot}$  and  $0.05 \pm 0.03M_{\odot}$  for SNe 2013hj and 2014G respectively.

We performed semi-analytical modelling of bolometric light curves of SNe 2013hj and 2014G to estimate explosion and progenitor properties. For SN 2013hj we estimate a progenitor mass of  $\sim 11M_{\odot}$  with a radius of  $\sim 700R_{\odot}$ , whereas for SN 2014G progenitor mass is estimated to  $\sim 9M_{\odot}$  with radius  $\sim 630M_{\odot}$ . The total explosion energy (kinetic + thermal) for both the SNe is approximately  $\sim 2 \text{ foe}$ . The steeper tail light curve of SN 2014G is fitted by reducing the effectiveness of gamma ray trapping parameter  $A_g$  in the model.

Broadband polarimetric observations of SNe 2013hj and 2014G are also presented in this paper. Even after considering maximum possible contamination in polarization due to host galaxy, SN 2013hj is found to reveal some intrinsic polarization in its light (specially during mid- to late-plateau phases), which may become significant on adopting lower host reddening or by changing host polarization angle. The temporal evolution of polarization shows subtle but monotonic increment as SN evolves towards plateau end. It is generally expected for stripped or partially stripped SNe, namely Type Ib/c or Iib, to exhibit higher degree of polarization as compared to SNe with hydrogen envelope intact as in IIPs. As both of our studied SNe are fast declining Type II events, some fraction of H envelope may have already been shredded during pre-SN evolution in the form of stellar winds, thus the explosion will have relatively less amount of hydrogen retained which will quickly start to reveal the central part having higher degree of asymmetry (Leonard & Filippenko 2005). Evidence of similar polarization enhancement in SNe IIP during plateau to early nebular phase has been also reported by Leonard et al. (2001, 2006) for SNe 1999em and 2004dj. On the other hand, polarization detected for SN 2014G in our observations is of very low significance, and it may be within the level of interstellar polarization due to the host galaxy.

## ACKNOWLEDGMENTS

We are thankful to the observers and observing staffs of ARIES and observatory of Osaka Kyoiku University for kind cooperation in observations of these objects. SB also acknowledges Dr. Eswaraiiah C. for useful discussion on AIMPOL observations and data. We gratefully acknowledge the services of the NASA ADS, NED and SOUSA which are used to access data and references in this paper. We also thank the referee for the useful comments and suggestions on the manuscript.

## REFERENCES

- Alard C., 2000, *A&AS*, 144, 363  
 Alard C., Lupton R. H., 1998, *ApJ*, 503, 325  
 Anderson J. P. et al., 2014, *ApJ*, 786, 67  
 Antezana R. et al., 2013, *Central Bureau Electronic Telegrams*, 3757, 1  
 Arnett W. D., 1980, *ApJ*, 237, 541  
 Arnett W. D., 1982, *ApJ*, 253, 785  
 Arnett W. D., Fu A., 1989, *ApJ*, 340, 396  
 Barbon R., Ciatti F., Rosino L., 1979, *A&A*, 72, 287  
 Barbon R., Ciatti F., Rosino L., 1982, *A&A*, 116, 35  
 Barbon R., Benetti S., Rosino L., Cappellaro E., Turatto M., 1990, *A&A*, 237, 79  
 Barrett P., 1988, *MNRAS*, 234, 937  
 Bayless A. J. et al., 2013, *ApJL*, 764, L13  
 Bersten M. C., Benvenuto O., Hamuy M., 2011, *ApJ*, 729, 61  
 Blondin S., Tonry J. L., 2007, *ApJ*, 666, 1024  
 Bose S., Kumar B., 2014, *ApJ*, 782, 98  
 Bose S. et al., 2013, *MNRAS*, 433, 1871  
 Bose S. et al., 2015a, *MNRAS*, 450, 2373  
 Bose S. et al., 2015b, *ApJ*, 806, 160  
 Breeveld A. A., Landsman W., Holland S. T., Roming P., Kuin N. P. M., Page M. J., 2011, in J.E. McEnery, J.L. Racusin, N. Gehrels, eds, *American Institute of Physics Conference Series. American Institute of Physics Conference Series*, Vol. 1358, pp. 373–376  
 Brown P. J., Breeveld A. A., Holland S., Kuin P., Pritchard T., 2014, *Ap&SS*, 354, 89  
 Brown P. J. et al., 2009, *AJ*, 137, 4517  
 Burrows A., 2013, *Reviews of Modern Physics*, 85, 245  
 Chatzopoulos E., Wheeler J. C., Vinko J., 2012, *ApJ*, 746, 121  
 Chugai N. N., 2006, *Astronomy Letters*, 32, 739  
 Clocchiatti A., Wheeler J. C., 1997, *ApJ*, 491, 375  
 Denisenko D. et al., 2014, *Central Bureau Electronic Telegrams*, 3787, 2  
 Dessart L. et al., 2008, *ApJ*, 675, 644  
 Eenmae T., Martin J. C., Grammer S., Humphreys R., 2014, *The Astronomer's Telegram*, 5935, 1  
 Elmhamdi A. et al., 2003, *MNRAS*, 338, 939  
 Eswaraiiah C., Maheswar G., Pandey A. K., Jose J., Ramaprakash A. N., Bhatt H. C., 2013, *A&A*, 556, A65  
 Falk S. W., Arnett W. D., 1977, *ApJS*, 33, 515  
 Faran T. et al., 2014, *MNRAS*, 445, 554  
 Filippenko A. V., 1997, *ARA&A*, 35, 309  
 Filippenko A. V., Foley R. J., 2005, *IAU Circ.*, 8484, 2  
 Gehrels N. et al., 2004, *ApJ*, 611, 1005  
 Hamuy M., 2003, *ApJ*, 582, 905  
 Hamuy M., Pinto P. A., 2002, *ApJL*, 566, L63  
 Hamuy M., Suntzeff N. B., 1990, *AJ*, 99, 1146  
 Han J., 2009, in K.G. Strassmeier, A.G. Kosovichev, J.E. Beckman, eds, *IAU Symposium. IAU Symposium*, Vol. 259, pp. 455–466  
 Harutyunyan A. H. et al., 2008, *A&A*, 488, 383  
 Heger A., Fryer C. L., Woosley S. E., Langer N., Hartmann D. H., 2003, *ApJ*, 591, 288  
 Heiles C., 2000, *AJ*, 119, 923  
 Hough J. H., Bailey J. A., Rouse M. F., Whittet D. C. B., 1987, *MNRAS*, 227, 1P  
 Inserra C. et al., 2012, *MNRAS*, 422, 1122  
 Jones M. I. et al., 2009, *ApJ*, 696, 1176  
 Kirshner R. P., Kwan J., 1974, *ApJ*, 193, 27  
 Kumar B., Pandey S. B., Eswaraiiah C., Gorosabel J., 2014, *MNRAS*, 442, 2  
 Landolt A. U., 2009, *AJ*, 137, 4186  
 Leonard D. C., Filippenko A. V., 2001, *PASP*, 113, 920  
 Leonard D. C., Filippenko A. V., 2005, in M. Turatto, S. Benetti, L. Zampieri, W. Shea, eds, *1604-2004: Supernovae as Cosmological Lighthouses. Astronomical Society of the Pacific Conference Series*, Vol. 342, p. 330  
 Leonard D. C., Filippenko A. V., Ardila D. R., Brotherton M. S., 2001, *ApJ*, 553, 861  
 Leonard D. C. et al., 2002a, *AJ*, 124, 2490  
 Leonard D. C. et al., 2002b, *PASP*, 114, 35  
 Leonard D. C. et al., 2006, *Nature*, 440, 505  
 Li W. et al., 2011, *MNRAS*, 412, 1441  
 Litvinova I. Y., Nadezhin D. K., 1985, *Soviet Astronomy Letters*, 11, 145  
 Makarov D., Prugniel P., Terekhova N., Courtois H., Vauglin I., 2014, *A&A*, 570, A13  
 Maund J. R., Wheeler J. C., Patat F., Wang L., Baade D., Höflich P. A., 2007, *ApJ*, 671, 1944  
 Nagy A. P., Ordasi A., Vinkó J., Wheeler J. C., 2014, *A&A*, 571, A77  
 Ochner P. et al., 2014, *The Astronomer's Telegram*, 5767, 1  
 Olivares E. F. et al., 2010, *ApJ*, 715, 833  
 Pastorello A. et al., 2009, *MNRAS*, 394, 2266  
 Pereyra A., Magalhães A. M., Rodrigues C. V., Silva C. R., Campos R., Hickel G., Cieslinski D., 2006, *A&A*, 454, 827  
 Popov D. V., 1993, *ApJ*, 414, 712  
 Poznanski D., Prochaska J. X., Bloom J. S., 2012, *MNRAS*, 426, 1465  
 Pumo M. L., Zampieri L., 2011, *ApJ*, 741, 41  
 Quimby R. M., Wheeler J. C., Höflich P., Akerlof C. W., Brown P. J., Rykoff E. S., 2007, *ApJ*, 666, 1093  
 Ramaprakash A. N., Gupta R., Sen A. K., Tandon S. N., 1998, *A&AS*, 128, 369  
 Rautela B. S., Joshi G. C., Pandey J. C., 2004, *Bulletin of the Astronomical Society of India*, 32, 159  
 Roming P. W. A. et al., 2005, *Space Sci. Rev.*, 120, 95  
 Sahu D. K., Anupama G. C., Srividya S., Muneer S., 2006, *MNRAS*, 372, 1315  
 Sanders N. E. et al., 2015, *ApJ*, 799, 208  
 Scarrott S. M., Rolph C. D., Semple D. P., 1990, in R. Beck, R. Wielebinski, P.P. Kronberg, eds, *Galactic and Inter-galactic Magnetic Fields. IAU Symposium*, Vol. 140, pp. 245–251

- Scarrott S. M., Rolph C. D., Wolstencroft R. W., Tadhunter C. N., 1991, MNRAS, 249, 16P
- Schlafly E. F., Finkbeiner D. P., 2011, ApJ, 737, 103
- Schmidt G. D., Elston R., Lupie O. L., 1992, AJ, 104, 1563
- Serkowski K., Mathewson D. S., Ford V. L., 1975, ApJ, 196, 261
- Smartt S. J., 2009, ARA&A, 47, 63
- Smartt S. J., Eldridge J. J., Crockett R. M., Maund J. R., 2009, MNRAS, 395, 1409
- Tomasella L. et al., 2013, MNRAS, 434, 1636
- Trammell S. R., Hines D. C., Wheeler J. C., 1993, ApJL, 414, L21
- Tran H. D., Filippenko A. V., Schmidt G. D., Bjorkman K. S., Jannuzi B. T., Smith P. S., 1997, PASP, 109, 489
- Tully R. B., Fisher J. R., 1988, Catalog of Nearby Galaxies
- Turatto M., Benetti S., Cappellaro E., 2003, in W. Hillebrandt, B. Leibundgut, eds, From Twilight to Highlight: The Physics of Supernovae. p. 200
- Utrobin V. P., 2007, A&A, 461, 233
- Valenti S. et al., 2014, MNRAS, 438, L101
- Valenti S. et al., 2015, MNRAS, 448, 2608
- Wang L., Wheeler J. C., 1996, ApJL, 462, L27
- Wang L., Wheeler J. C., 2008, ARA&A, 46, 433
- Wang L., Howell D. A., Höflich P., Wheeler J. C., 2001, ApJ, 550, 1030
- Wang L., Baade D., Höflich P., Wheeler J. C., 2002a, The Messenger, 109, 47
- Wang L. et al., 2002b, ApJ, 579, 671
- Wang L. et al., 2003, ApJ, 591, 1110
- Zampieri L., Pastorello A., Turatto M., Cappellaro E., Benetti S., Altavilla G., Mazzali P., Hamuy M., 2003, MNRAS, 338, 711

## APPENDIX A: TABLES OF PHOTOMETRY

**Table A1.** Calibrated secondary standards in the fields of SNe 2013hj and 2014G with corresponding coordinates ( $\alpha, \delta$ ) and calibrated magnitudes in *UBVRI* bands are listed. Errors quoted here include both photometric and calibration errors.

SN 2013hj field standards							
Star ID	$\alpha_{J2000}$ (h m s)	$\delta_{J2000}$ ( $^{\circ}$ ' ")	<i>U</i> (mag)	<i>B</i> (mag)	<i>V</i> (mag)	<i>R</i> (mag)	<i>I</i> (mag)
A	9:11:51.9	-15:26:02.4	18.116 $\pm$ 0.071	17.272 $\pm$ 0.021	16.355 $\pm$ 0.012	15.824 $\pm$ 0.007	15.399 $\pm$ 0.024
B	9:12:01.2	-15:26:30.1	16.972 $\pm$ 0.032	17.011 $\pm$ 0.009	16.455 $\pm$ 0.010	16.136 $\pm$ 0.018	15.831 $\pm$ 0.022
C	9:11:57.3	-15:28:20.6	18.496 $\pm$ 0.114	18.896 $\pm$ 0.023	18.285 $\pm$ 0.021	17.934 $\pm$ 0.013	17.607 $\pm$ 0.030
D	9:12:03.3	-15:27:09.8	16.320 $\pm$ 0.013	16.414 $\pm$ 0.007	16.003 $\pm$ 0.009	15.742 $\pm$ 0.009	15.509 $\pm$ 0.017
E	9:12:06.5	-15:26:28.6	—	19.144 $\pm$ 0.065	17.857 $\pm$ 0.021	17.056 $\pm$ 0.027	16.380 $\pm$ 0.022
F	9:12:01.8	-15:29:00.0	13.942 $\pm$ 0.010	13.615 $\pm$ 0.013	12.833 $\pm$ 0.015	12.311 $\pm$ 0.015	11.917 $\pm$ 0.062
G	9:12:09.0	-15:27:32.0	18.843 $\pm$ 0.110	18.105 $\pm$ 0.019	17.144 $\pm$ 0.009	16.551 $\pm$ 0.009	16.084 $\pm$ 0.034
H	9:12:11.7	-15:28:33.6	17.775 $\pm$ 0.065	16.867 $\pm$ 0.006	15.870 $\pm$ 0.010	15.308 $\pm$ 0.008	14.872 $\pm$ 0.018
I	9:12:20.0	-15:24:01.5	17.886 $\pm$ 0.085	17.959 $\pm$ 0.025	17.459 $\pm$ 0.023	17.090 $\pm$ 0.023	16.804 $\pm$ 0.019
J	9:12:17.9	-15:22:52.8	18.224 $\pm$ 0.095	17.938 $\pm$ 0.012	17.154 $\pm$ 0.015	16.727 $\pm$ 0.008	16.390 $\pm$ 0.017
K	9:12:14.3	-15:22:54.7	16.526 $\pm$ 0.017	16.024 $\pm$ 0.008	15.135 $\pm$ 0.010	14.620 $\pm$ 0.024	14.194 $\pm$ 0.014
L	9:12:06.7	-15:24:58.8	17.013 $\pm$ 0.027	17.041 $\pm$ 0.011	16.406 $\pm$ 0.012	16.043 $\pm$ 0.007	15.711 $\pm$ 0.021
M	9:12:09.6	-15:21:45.3	15.877 $\pm$ 0.010	15.860 $\pm$ 0.006	15.300 $\pm$ 0.012	14.944 $\pm$ 0.008	14.630 $\pm$ 0.013
N	9:11:57.9	-15:23:46.1	17.402 $\pm$ 0.028	17.060 $\pm$ 0.010	16.328 $\pm$ 0.014	15.901 $\pm$ 0.007	15.533 $\pm$ 0.029
O	9:11:57.7	-15:25:17.1	—	18.942 $\pm$ 0.026	18.008 $\pm$ 0.027	17.399 $\pm$ 0.009	16.920 $\pm$ 0.023
P	9:12:06.0	-15:24:15.8	11.697 $\pm$ 0.006	11.660 $\pm$ 0.006	11.060 $\pm$ 0.031	—	—
Q	9:12:08.6	-15:26:57.0	12.162 $\pm$ 0.004	12.063 $\pm$ 0.005	11.796 $\pm$ 0.022	11.606 $\pm$ 0.015	11.442 $\pm$ 0.062
SN 2014G field standards							
A	10:54:26.8	54:16:47.1	19.934 $\pm$ 0.456	18.943 $\pm$ 0.020	17.862 $\pm$ 0.020	17.238 $\pm$ 0.035	16.722 $\pm$ 0.042
B	10:54:32.0	54:14:28.0	17.940 $\pm$ 0.044	17.854 $\pm$ 0.020	17.253 $\pm$ 0.016	16.880 $\pm$ 0.026	16.496 $\pm$ 0.030
C	10:54:42.6	54:17:03.7	19.067 $\pm$ 0.080	18.648 $\pm$ 0.019	17.787 $\pm$ 0.023	17.284 $\pm$ 0.033	16.818 $\pm$ 0.041
D	10:54:52.6	54:13:53.8	16.133 $\pm$ 0.022	16.106 $\pm$ 0.015	15.500 $\pm$ 0.018	15.144 $\pm$ 0.028	14.839 $\pm$ 0.031
E	10:54:59.9	54:15:21.2	17.539 $\pm$ 0.024	17.626 $\pm$ 0.012	17.067 $\pm$ 0.014	16.714 $\pm$ 0.027	16.402 $\pm$ 0.039
F	10:54:58.9	54:17:19.9	15.753 $\pm$ 0.009	15.141 $\pm$ 0.011	14.274 $\pm$ 0.016	13.754 $\pm$ 0.028	13.382 $\pm$ 0.039
G	10:55:10.7	54:17:52.9	18.910 $\pm$ 0.097	17.656 $\pm$ 0.027	16.502 $\pm$ 0.017	15.796 $\pm$ 0.032	15.199 $\pm$ 0.025
H	10:55:04.1	54:22:09.0	18.734 $\pm$ 0.107	18.595 $\pm$ 0.042	17.850 $\pm$ 0.019	17.445 $\pm$ 0.033	17.061 $\pm$ 0.023
I	10:54:55.1	54:21:18.4	18.482 $\pm$ 0.062	18.552 $\pm$ 0.024	17.894 $\pm$ 0.020	17.533 $\pm$ 0.021	17.200 $\pm$ 0.023
J	10:54:45.1	54:20:45.1	—	19.994 $\pm$ 0.099	18.608 $\pm$ 0.031	17.746 $\pm$ 0.024	16.995 $\pm$ 0.024
K	10:54:36.8	54:21:35.4	16.861 $\pm$ 0.013	16.252 $\pm$ 0.021	15.395 $\pm$ 0.017	14.899 $\pm$ 0.025	14.491 $\pm$ 0.024
L	10:54:37.0	54:23:42.9	18.337 $\pm$ 0.060	18.915 $\pm$ 0.026	18.633 $\pm$ 0.045	18.191 $\pm$ 0.038	17.843 $\pm$ 0.038
M	10:54:30.3	54:20:16.0	—	19.328 $\pm$ 0.025	17.987 $\pm$ 0.026	17.215 $\pm$ 0.024	16.566 $\pm$ 0.035
N	10:54:28.0	54:20:54.3	16.065 $\pm$ 0.018	16.137 $\pm$ 0.013	15.637 $\pm$ 0.016	15.309 $\pm$ 0.026	15.023 $\pm$ 0.028
O	10:54:22.6	54:19:00.3	15.632 $\pm$ 0.014	15.407 $\pm$ 0.013	14.750 $\pm$ 0.014	14.362 $\pm$ 0.030	14.048 $\pm$ 0.034
P	10:54:07.0	54:19:03.0	17.292 $\pm$ 0.024	17.089 $\pm$ 0.012	16.409 $\pm$ 0.023	15.976 $\pm$ 0.027	15.590 $\pm$ 0.032
Q	10:54:01.6	54:18:04.5	18.828 $\pm$ 0.169	18.030 $\pm$ 0.035	17.049 $\pm$ 0.020	16.454 $\pm$ 0.030	15.865 $\pm$ 0.034

Table A2: Photometric evolution of SN 2013hj in *UBVRI* bands.

UT Date (yyyy-mm-dd)	JD 2456000+	Phase <sup>a</sup> (day)	<i>U</i> (mag)	<i>B</i> (mag)	<i>V</i> (mag)	<i>R</i> (mag)	<i>I</i> (mag)	Tel <sup>b</sup>
2013-12-13.88	640.38	3.38	13.681 ± 0.041	14.700 ± 0.024	14.819 ± 0.016	14.806 ± 0.016	14.858 ± 0.034	ARIES
2013-12-14.84	641.34	4.34	13.721 ± 0.025	14.702 ± 0.014	14.757 ± 0.010	14.716 ± 0.010	14.743 ± 0.020	ARIES
2013-12-15.92	642.42	5.42	13.739 ± 0.028	14.699 ± 0.017	14.696 ± 0.011	14.633 ± 0.011	14.639 ± 0.023	ARIES
2013-12-16.93	643.43	6.43	13.775 ± 0.028	14.694 ± 0.024	14.667 ± 0.016	14.565 ± 0.015	14.546 ± 0.031	ARIES
2013-12-18.79	645.29	8.29	13.849 ± 0.042	14.738 ± 0.024	14.632 ± 0.016	14.492 ± 0.015	14.441 ± 0.031	ARIES
2013-12-19.80	646.30	9.30	13.899 ± 0.030	14.769 ± 0.018	14.653 ± 0.012	14.496 ± 0.011	14.412 ± 0.021	ARIES
2013-12-21.01	647.51	10.51	13.924 ± 0.047	14.758 ± 0.026	14.652 ± 0.018	14.505 ± 0.016	14.388 ± 0.034	ARIES
2013-12-25.83	652.33	15.33	14.151 ± 0.021	14.892 ± 0.017	14.730 ± 0.010	14.496 ± 0.011	14.412 ± 0.023	ARIES
2013-12-28.72	655.22	18.22	—	—	14.785 ± 0.012	14.558 ± 0.013	—	OKU
2013-12-28.83	655.33	18.33	14.281 ± 0.029	14.943 ± 0.017	14.738 ± 0.012	14.516 ± 0.011	14.447 ± 0.023	ARIES
2013-12-29.73	656.23	19.23	—	—	14.783 ± 0.008	14.579 ± 0.008	—	OKU
2013-12-29.91	656.41	19.41	14.371 ± 0.029	14.969 ± 0.017	14.753 ± 0.011	—	14.467 ± 0.023	ARIES
2013-12-31.69	658.19	21.19	—	—	—	—	14.490 ± 0.033	OKU
2014-01-01.66	659.16	22.16	—	—	14.835 ± 0.008	14.582 ± 0.008	—	OKU
2014-01-02.69	660.19	23.19	—	—	14.829 ± 0.008	14.598 ± 0.009	—	OKU
2014-01-03.68	661.18	24.18	—	—	14.848 ± 0.008	14.608 ± 0.009	—	OKU
2014-01-05.61	663.11	26.11	—	—	14.849 ± 0.009	14.576 ± 0.007	—	OKU
2014-01-06.61	664.11	27.11	—	15.304 ± 0.015	—	—	14.487 ± 0.015	OKU
2014-01-06.86	664.36	27.36	—	15.280 ± 0.018	14.919 ± 0.012	14.606 ± 0.011	14.515 ± 0.023	ARIES
2014-01-07.73	665.23	28.23	—	—	14.890 ± 0.014	—	14.481 ± 0.022	OKU
2014-01-09.72	667.22	30.22	—	—	—	14.587 ± 0.010	14.489 ± 0.026	OKU
2014-01-10.56	668.06	31.06	—	—	14.928 ± 0.010	14.632 ± 0.009	—	OKU
2014-01-11.59	669.09	32.09	—	—	—	—	14.491 ± 0.012	OKU
2014-01-11.97	669.47	32.47	15.610 ± 0.037	15.519 ± 0.026	14.969 ± 0.016	14.622 ± 0.015	14.527 ± 0.032	ARIES
2014-01-12.79	670.29	33.29	15.695 ± 0.037	15.568 ± 0.020	14.969 ± 0.012	14.626 ± 0.009	14.516 ± 0.023	ARIES
2014-01-13.66	671.16	34.16	—	—	14.981 ± 0.007	—	—	OKU
2014-01-14.80	672.30	35.30	—	—	—	14.633 ± 0.015	14.533 ± 0.031	ARIES
2014-01-15.64	673.14	36.14	—	15.700 ± 0.017	14.989 ± 0.009	—	—	OKU
2014-01-15.93	673.43	36.43	15.854 ± 0.048	—	14.995 ± 0.017	14.642 ± 0.015	14.547 ± 0.032	ARIES
2014-01-16.71	674.21	37.21	—	15.782 ± 0.039	—	14.650 ± 0.009	14.503 ± 0.020	OKU
2014-01-16.82	674.32	37.32	16.073 ± 0.042	15.744 ± 0.021	15.017 ± 0.012	14.649 ± 0.011	14.541 ± 0.023	ARIES
2014-01-17.71	675.21	38.21	—	—	15.038 ± 0.011	14.663 ± 0.011	—	OKU
2014-01-18.83	676.33	39.33	—	—	—	—	14.504 ± 0.021	OKU
2014-01-19.71	677.21	40.21	—	15.833 ± 0.021	15.077 ± 0.011	14.691 ± 0.011	—	OKU
2014-01-20.85	678.35	41.35	16.418 ± 0.051	15.879 ± 0.019	15.092 ± 0.010	14.687 ± 0.010	14.517 ± 0.015	ARIES
2014-01-21.71	679.21	42.21	—	—	15.116 ± 0.021	14.706 ± 0.038	14.532 ± 0.021	OKU
2014-01-23.75	681.25	44.25	—	15.995 ± 0.020	15.155 ± 0.010	—	—	OKU
2014-01-24.80	682.30	45.30	—	—	—	—	14.590 ± 0.017	OKU
2014-01-24.84	682.34	45.34	16.774 ± 0.047	15.963 ± 0.022	15.237 ± 0.013	14.783 ± 0.010	14.568 ± 0.023	ARIES
2014-01-25.83	683.33	46.33	16.627 ± 0.087	15.982 ± 0.029	15.148 ± 0.016	14.683 ± 0.015	14.566 ± 0.031	ARIES
2014-01-26.82	684.32	47.32	16.687 ± 0.061	16.018 ± 0.028	15.168 ± 0.016	14.694 ± 0.015	14.577 ± 0.031	ARIES
2014-01-27.74	685.24	48.24	—	16.095 ± 0.022	15.202 ± 0.010	—	—	OKU
2014-01-28.75	686.25	49.25	—	—	—	14.739 ± 0.009	14.579 ± 0.017	OKU
2014-01-28.90	686.40	49.40	16.890 ± 0.098	16.157 ± 0.024	15.207 ± 0.013	14.742 ± 0.013	14.611 ± 0.020	ARIES
2014-01-29.84	687.34	50.34	16.879 ± 0.068	16.118 ± 0.030	15.210 ± 0.016	14.720 ± 0.015	14.596 ± 0.031	ARIES
2014-01-30.82	688.32	51.32	17.009 ± 0.065	16.215 ± 0.025	15.247 ± 0.011	14.775 ± 0.012	14.633 ± 0.023	ARIES
2014-01-31.73	689.23	52.23	—	16.324 ± 0.033	—	—	—	OKU
2014-01-31.80	689.30	52.30	17.049 ± 0.064	16.266 ± 0.031	15.270 ± 0.016	14.778 ± 0.015	14.641 ± 0.031	ARIES
2014-02-01.78	690.28	53.28	17.093 ± 0.064	16.279 ± 0.026	15.276 ± 0.013	14.788 ± 0.012	14.642 ± 0.023	ARIES
2014-02-02.76	691.26	54.26	17.152 ± 0.070	16.322 ± 0.033	15.300 ± 0.016	14.798 ± 0.015	14.645 ± 0.031	ARIES
2014-02-05.76	694.26	57.26	—	16.310 ± 0.027	15.323 ± 0.012	—	—	OKU
2014-02-05.84	694.34	57.34	17.300 ± 0.089	16.306 ± 0.032	15.313 ± 0.017	14.776 ± 0.015	14.628 ± 0.032	ARIES
2014-02-09.71	698.21	61.21	—	—	15.370 ± 0.013	14.826 ± 0.035	—	OKU
2014-02-09.79	698.29	61.29	17.510 ± 0.104	16.510 ± 0.036	15.403 ± 0.013	14.868 ± 0.016	14.722 ± 0.031	ARIES
2014-02-10.69	699.19	62.19	—	—	—	14.859 ± 0.009	14.682 ± 0.019	OKU
2014-02-11.82	700.32	63.32	17.701 ± 0.118	16.573 ± 0.030	15.430 ± 0.011	14.895 ± 0.012	14.734 ± 0.024	ARIES
2014-02-12.87	701.37	64.37	17.708 ± 0.144	16.543 ± 0.031	15.439 ± 0.011	14.896 ± 0.010	14.748 ± 0.020	ARIES
2014-02-16.75	705.25	68.25	17.619 ± 0.120	16.664 ± 0.035	15.502 ± 0.014	14.941 ± 0.012	14.779 ± 0.024	ARIES
2014-02-17.74	706.24	69.24	17.894 ± 0.132	16.728 ± 0.035	15.515 ± 0.013	14.941 ± 0.012	14.764 ± 0.024	ARIES
2014-02-19.57	708.07	71.07	—	—	—	15.006 ± 0.013	—	OKU
2014-02-19.86	708.36	71.36	17.910 ± 0.173	16.757 ± 0.037	15.567 ± 0.018	14.975 ± 0.016	14.807 ± 0.033	ARIES
2014-02-20.72	709.22	72.22	—	—	—	14.975 ± 0.010	14.813 ± 0.019	OKU
2014-02-21.69	710.19	73.19	18.064 ± 0.138	16.705 ± 0.032	15.607 ± 0.018	14.967 ± 0.016	14.798 ± 0.024	ARIES
2014-02-22.75	711.25	74.25	18.163 ± 0.156	16.754 ± 0.040	15.619 ± 0.018	14.976 ± 0.016	14.808 ± 0.024	ARIES
2014-02-23.75	712.25	75.25	—	—	—	—	—	OKU
2014-02-24.61	713.11	76.11	—	16.793 ± 0.039	15.619 ± 0.013	—	—	OKU
2014-02-25.64	714.14	77.14	—	—	15.627 ± 0.018	15.059 ± 0.015	—	OKU
2014-02-25.80	714.30	77.30	18.080 ± 0.181	16.901 ± 0.050	15.608 ± 0.018	15.047 ± 0.013	14.862 ± 0.024	ARIES
2014-03-02.70	719.20	82.20	18.537 ± 0.220	17.071 ± 0.045	15.732 ± 0.015	15.147 ± 0.013	14.943 ± 0.024	ARIES
2014-03-03.62	720.12	83.12	—	—	15.851 ± 0.016	—	—	OKU
2014-03-05.69	722.19	85.19	—	—	—	—	14.985 ± 0.054	OKU
2014-03-07.68	724.18	87.18	—	—	15.907 ± 0.019	15.274 ± 0.019	—	OKU
2014-03-07.69	724.19	87.19	18.786 ± 0.266	17.292 ± 0.053	15.910 ± 0.016	15.229 ± 0.013	15.037 ± 0.025	ARIES
2014-03-08.73	725.23	88.23	18.852 ± 0.293	17.336 ± 0.052	15.942 ± 0.017	15.262 ± 0.013	15.064 ± 0.034	ARIES
2014-03-10.55	727.05	90.05	—	—	15.995 ± 0.020	15.311 ± 0.012	—	OKU
2014-03-11.67	728.17	91.17	—	—	16.003 ± 0.025	15.358 ± 0.019	—	OKU
2014-03-12.76	729.26	92.26	—	17.478 ± 0.065	16.065 ± 0.022	15.365 ± 0.018	15.143 ± 0.027	ARIES
2014-03-13.68	730.18	93.18	18.927 ± 0.393	17.565 ± 0.069	16.095 ± 0.018	15.381 ± 0.015	15.165 ± 0.026	ARIES
2014-03-14.62	731.12	94.12	—	—	16.187 ± 0.019	15.388 ± 0.023	—	OKU
2014-03-14.83	731.33	94.33	—	17.561 ± 0.076	16.116 ± 0.019	15.434 ± 0.013	15.204 ± 0.023	ARIES
2014-03-16.80	733.30	96.30	—	17.740 ± 0.094	16.209 ± 0.020	15.460 ± 0.014	15.254 ± 0.028	ARIES
2014-03-18.67	735.17	98.17	—	17.787 ± 0.086	16.244 ± 0.024	15.551 ± 0.018	15.313 ± 0.028	ARIES
2014-03-19.67	736.17	99.17	18.781 ± 0.317	17.853 ± 0.088	16.319 ± 0.021	15.572 ± 0.017	15.351 ± 0.028	ARIES
2014-03-20.67	737.17	100.17	19.102 ± 0.361	17.909 ± 0.089	16.388 ± 0.021	15.620 ± 0.015	15.390 ± 0.025	ARIES
2014-03-23.62	740.12	103.12	—	—	—	15.827 ± 0.021	15.532 ± 0.031	OKU
2014-03-23.79	740.29	103.29	—	18.099 ± 0.107	16.564 ± 0.030	15.761 ± 0.022	15.550 ± 0.039	ARIES
2014-03-27.63	744.13	107.13	—	—	—	16.095 ± 0.030	15.811 ± 0.033	OKU
2014-03-31.63	748.13	111.13	—	—	—	16.357 ± 0.030	16.250 ± 0.046	OKU

Table A2 - continued.

UT Date (yyyy-mm-dd)	JD 2456000+	Phase <sup>a</sup> (day)	<i>U</i> (mag)	<i>B</i> (mag)	<i>V</i> (mag)	<i>R</i> (mag)	<i>I</i> (mag)	Tel <sup>b</sup>
2014-04-01.61	749.11	112.11	—	—	—	16.448 ± 0.050	—	OKU
2014-04-02.59	750.09	113.09	—	18.897 ± 0.217	17.533 ± 0.066	16.581 ± 0.038	16.324 ± 0.057	ARIES
2014-04-06.60	754.10	117.10	—	—	—	16.672 ± 0.038	—	OKU
2014-04-07.62	755.12	118.12	—	—	—	—	16.387 ± 0.053	OKU
2014-04-07.73	755.23	118.23	—	—	17.699 ± 0.070	16.723 ± 0.041	16.438 ± 0.054	ARIES
2014-04-08.57	756.07	119.07	—	—	—	16.737 ± 0.046	—	OKU
2014-04-08.63	756.13	119.13	—	19.141 ± 0.268	17.809 ± 0.071	16.789 ± 0.039	16.516 ± 0.056	ARIES
2014-04-09.57	757.07	120.07	—	—	—	16.829 ± 0.047	—	OKU
2014-04-09.62	757.12	120.12	—	19.218 ± 0.303	17.866 ± 0.081	16.831 ± 0.044	16.555 ± 0.061	ARIES
2014-04-11.47	758.97	121.97	—	—	—	16.833 ± 0.052	—	OKU
2014-04-11.72	759.22	122.22	—	18.986 ± 0.289	17.722 ± 0.079	16.765 ± 0.039	16.522 ± 0.061	ARIES
2014-04-12.56	760.06	123.06	—	—	—	—	—	OKU
2014-04-14.65	762.15	125.15	—	19.470 ± 0.409	17.755 ± 0.070	16.842 ± 0.043	16.563 ± 0.055	ARIES
2014-04-19.68	767.18	130.18	19.739 ± 0.707	19.592 ± 0.418	17.847 ± 0.071	16.875 ± 0.044	16.612 ± 0.061	ARIES
2014-04-20.65	768.15	131.15	—	19.274 ± 0.301	17.958 ± 0.080	16.897 ± 0.043	16.636 ± 0.063	ARIES
2014-04-21.64	769.14	132.14	20.197 ± 0.955	19.281 ± 0.307	17.920 ± 0.077	16.894 ± 0.049	16.638 ± 0.061	ARIES
2014-04-23.55	771.05	134.05	—	—	—	—	16.617 ± 0.063	OKU
2014-04-26.74	774.24	137.24	—	19.490 ± 0.477	17.986 ± 0.112	16.910 ± 0.047	16.619 ± 0.063	ARIES
2014-04-27.63	775.13	138.13	19.730 ± 0.809	19.457 ± 0.390	17.906 ± 0.089	16.941 ± 0.046	16.635 ± 0.063	ARIES
2014-05-09.63	787.13	150.13	—	19.409 ± 0.473	18.021 ± 0.095	17.003 ± 0.055	16.693 ± 0.064	ARIES
2014-05-10.63	788.13	151.13	—	—	18.063 ± 0.093	17.061 ± 0.052	16.724 ± 0.073	ARIES
2014-05-13.63	791.13	154.13	—	19.081 ± 0.401	17.975 ± 0.086	17.096 ± 0.061	16.917 ± 0.089	ARIES
2014-05-15.64	793.14	156.14	—	19.276 ± 0.355	17.947 ± 0.089	17.128 ± 0.061	16.709 ± 0.072	ARIES
2014-05-16.62	794.12	157.12	—	19.408 ± 0.366	17.923 ± 0.087	17.093 ± 0.057	16.759 ± 0.072	ARIES
2014-05-20.62	798.12	161.12	—	19.469 ± 0.362	18.233 ± 0.104	17.165 ± 0.056	16.894 ± 0.076	ARIES
2014-05-21.63	799.13	162.13	—	19.436 ± 0.361	18.253 ± 0.108	17.165 ± 0.056	16.868 ± 0.076	ARIES
2014-05-26.63	804.13	167.13	—	—	18.075 ± 0.098	17.103 ± 0.060	16.818 ± 0.079	ARIES
2014-05-29.63	807.13	170.13	—	—	18.138 ± 0.095	17.165 ± 0.061	16.939 ± 0.086	ARIES

<sup>a</sup> with reference to the explosion epoch JD=2456637.0d<sup>b</sup> ARIES: 104cm Sampurnanand telescope and 130cm Devasthal fast optical telescope at ARIES, Nainital, India; OKU: 51cm telescope at Osaka Kyoiku University, Japan

Note: Data observed within 5 Hrs, are represented under single epoch observation.

**Table A3.** Photometric evolution of SN 2014G.

<i>UBVRI</i> photometry									
UT Date (yyyy-mm-dd)	JD 2456000+	Phase <sup>a</sup> (day)	<i>U</i> (mag)	<i>B</i> (mag)	<i>V</i> (mag)	<i>R</i> (mag)	<i>I</i> (mag)	Tel <sup>b</sup>	
2014-01-15.97	673.47	3.74	14.215 ± 0.040	15.043 ± 0.023	15.007 ± 0.017	14.924 ± 0.017	14.900 ± 0.033	ARIES	
2014-01-16.88	674.38	4.65	14.085 ± 0.028	14.911 ± 0.016	14.851 ± 0.013	14.738 ± 0.012	14.693 ± 0.020	ARIES	
2014-01-20.92	678.42	8.69	14.110 ± 0.029	14.829 ± 0.016	14.601 ± 0.012	14.436 ± 0.011	14.311 ± 0.022	ARIES	
2014-01-24.92	682.42	12.69	14.310 ± 0.028	14.860 ± 0.016	14.451 ± 0.011	—	14.064 ± 0.022	ARIES	
2014-01-25.93	683.43	13.70	14.294 ± 0.019	14.867 ± 0.014	14.472 ± 0.010	14.213 ± 0.012	14.067 ± 0.020	ARIES	
2014-01-27.91	685.41	15.68	14.441 ± 0.040	14.916 ± 0.023	14.465 ± 0.016	—	13.997 ± 0.030	ARIES	
2014-01-28.89	686.39	16.66	14.534 ± 0.030	14.996 ± 0.016	14.561 ± 0.012	14.263 ± 0.011	14.023 ± 0.022	ARIES	
2014-01-29.89	687.39	17.66	14.599 ± 0.040	15.007 ± 0.023	14.516 ± 0.016	14.206 ± 0.015	14.006 ± 0.030	ARIES	
2014-01-30.91	688.41	18.68	14.689 ± 0.029	15.073 ± 0.016	14.609 ± 0.011	14.296 ± 0.011	14.044 ± 0.022	ARIES	
2014-01-31.83	689.33	19.60	14.780 ± 0.029	15.143 ± 0.023	14.644 ± 0.016	14.308 ± 0.015	14.052 ± 0.030	ARIES	
2014-02-01.84	690.34	20.61	14.859 ± 0.023	15.185 ± 0.016	14.676 ± 0.011	14.320 ± 0.011	14.062 ± 0.022	ARIES	
2014-02-02.86	691.36	21.63	14.954 ± 0.025	15.245 ± 0.019	14.686 ± 0.014	14.344 ± 0.011	14.084 ± 0.022	ARIES	
2014-02-08.94	697.44	27.71	—	—	—	—	—	ARIES	
2014-02-09.82	698.32	28.59	15.662 ± 0.032	15.658 ± 0.017	14.962 ± 0.013	14.555 ± 0.012	14.270 ± 0.022	ARIES	
2014-02-11.88	700.38	30.65	15.890 ± 0.049	15.816 ± 0.017	15.051 ± 0.013	14.624 ± 0.012	14.331 ± 0.022	ARIES	
2014-02-12.91	701.41	31.68	16.013 ± 0.034	15.860 ± 0.024	15.064 ± 0.017	14.636 ± 0.015	14.333 ± 0.030	ARIES	
2014-02-16.81	705.31	35.58	16.467 ± 0.045	16.087 ± 0.020	15.231 ± 0.014	14.751 ± 0.013	14.447 ± 0.023	ARIES	
2014-02-17.80	706.30	36.57	16.516 ± 0.034	16.138 ± 0.019	15.232 ± 0.014	14.728 ± 0.012	14.423 ± 0.023	ARIES	
2014-02-19.89	708.39	38.66	16.814 ± 0.046	16.263 ± 0.019	15.314 ± 0.019	14.818 ± 0.017	14.491 ± 0.031	ARIES	
2014-02-21.74	710.24	40.51	16.910 ± 0.040	16.287 ± 0.020	15.365 ± 0.020	14.798 ± 0.017	14.498 ± 0.031	ARIES	
2014-02-22.78	711.28	41.55	16.968 ± 0.042	16.331 ± 0.027	15.397 ± 0.019	14.817 ± 0.016	14.512 ± 0.031	ARIES	
2014-02-25.84	714.34	44.61	17.399 ± 0.065	16.565 ± 0.022	15.469 ± 0.020	14.955 ± 0.017	14.601 ± 0.032	ARIES	
2014-03-02.77	719.27	49.54	17.705 ± 0.060	16.722 ± 0.023	15.616 ± 0.017	15.078 ± 0.014	14.710 ± 0.023	ARIES	
2014-03-07.76	724.26	54.53	17.957 ± 0.063	16.940 ± 0.025	15.768 ± 0.019	15.151 ± 0.015	14.804 ± 0.024	ARIES	
2014-03-08.77	725.27	55.54	18.019 ± 0.075	16.985 ± 0.024	15.784 ± 0.022	15.173 ± 0.018	14.816 ± 0.032	ARIES	
2014-03-12.79	729.29	59.56	18.301 ± 0.113	17.112 ± 0.036	15.879 ± 0.024	15.193 ± 0.018	14.884 ± 0.024	ARIES	
2014-03-13.75	730.25	60.52	18.428 ± 0.113	17.160 ± 0.027	15.892 ± 0.021	15.247 ± 0.015	14.887 ± 0.024	ARIES	
2014-03-14.87	731.37	61.64	18.596 ± 0.169	17.175 ± 0.039	15.914 ± 0.024	15.266 ± 0.019	14.916 ± 0.033	ARIES	
2014-03-16.83	733.33	63.60	18.276 ± 0.167	17.243 ± 0.031	15.957 ± 0.026	15.294 ± 0.020	14.931 ± 0.033	ARIES	
2014-03-18.72	735.22	65.49	18.426 ± 0.142	17.287 ± 0.033	15.997 ± 0.022	15.321 ± 0.017	14.962 ± 0.025	ARIES	
2014-03-19.73	736.23	66.50	18.659 ± 0.156	17.306 ± 0.032	16.006 ± 0.023	15.335 ± 0.017	14.980 ± 0.026	ARIES	
2014-03-20.71	737.21	67.48	18.931 ± 0.244	17.356 ± 0.042	16.045 ± 0.027	15.371 ± 0.020	15.013 ± 0.033	ARIES	
2014-03-21.71	738.21	68.48	18.706 ± 0.132	17.373 ± 0.032	16.046 ± 0.027	15.375 ± 0.021	15.021 ± 0.034	ARIES	
2014-03-22.82	739.32	69.59	18.712 ± 0.173	17.406 ± 0.041	16.096 ± 0.027	15.398 ± 0.020	15.046 ± 0.034	ARIES	
2014-03-23.82	740.32	70.59	18.825 ± 0.175	17.505 ± 0.054	—	—	15.070 ± 0.034	ARIES	
2014-03-29.87	746.37	76.64	—	—	16.350 ± 0.033	15.554 ± 0.022	15.181 ± 0.035	ARIES	
2014-04-02.62	750.12	80.39	—	17.814 ± 0.048	16.532 ± 0.039	15.705 ± 0.025	15.291 ± 0.037	ARIES	
2014-04-07.76	755.26	85.53	—	18.420 ± 0.100	17.025 ± 0.057	16.107 ± 0.033	15.648 ± 0.042	ARIES	
2014-04-08.70	756.20	86.47	19.576 ± 0.295	18.437 ± 0.075	17.222 ± 0.061	16.227 ± 0.031	15.756 ± 0.035	ARIES	
2014-04-09.84	757.34	87.61	20.295 ± 0.582	18.610 ± 0.091	17.436 ± 0.083	16.388 ± 0.041	15.902 ± 0.047	ARIES	
2014-04-11.76	759.26	89.53	—	18.967 ± 0.104	17.586 ± 0.084	16.587 ± 0.043	16.080 ± 0.044	ARIES	
2014-04-13.73	761.23	91.50	—	—	17.863 ± 0.124	—	—	ARIES	
2014-04-14.69	762.19	92.46	—	19.200 ± 0.149	17.952 ± 0.117	16.824 ± 0.052	16.306 ± 0.052	ARIES	
2014-04-19.72	767.22	97.49	20.076 ± 0.485	19.064 ± 0.133	18.032 ± 0.141	16.943 ± 0.067	16.451 ± 0.069	ARIES	
2014-04-20.71	768.21	98.48	19.719 ± 0.302	18.988 ± 0.121	18.125 ± 0.133	16.958 ± 0.059	16.440 ± 0.057	ARIES	
2014-04-21.71	769.21	99.48	19.580 ± 0.260	19.074 ± 0.126	18.123 ± 0.138	16.973 ± 0.060	16.482 ± 0.059	ARIES	
2014-04-25.80	773.30	103.57	—	19.137 ± 0.131	18.106 ± 0.156	17.007 ± 0.073	16.516 ± 0.073	ARIES	
2014-04-26.70	774.20	104.47	—	19.178 ± 0.128	18.148 ± 0.140	17.056 ± 0.064	16.555 ± 0.063	ARIES	
2014-04-28.65	776.15	106.42	20.818 ± 1.294	19.074 ± 0.142	18.175 ± 0.163	17.040 ± 0.077	16.597 ± 0.080	ARIES	
2014-05-04.69	782.19	112.46	20.558 ± 1.027	19.352 ± 0.175	18.311 ± 0.180	17.121 ± 0.081	16.638 ± 0.082	ARIES	
2014-05-09.67	787.17	117.44	—	19.530 ± 0.176	18.429 ± 0.186	17.225 ± 0.077	16.754 ± 0.078	ARIES	
2014-05-10.68	788.18	118.45	—	19.738 ± 0.238	18.399 ± 0.182	17.257 ± 0.080	16.796 ± 0.080	ARIES	
2014-05-13.67	791.17	121.44	—	19.647 ± 0.221	18.433 ± 0.213	17.292 ± 0.092	16.869 ± 0.097	ARIES	
2014-05-15.68	793.18	123.45	—	19.524 ± 0.215	18.516 ± 0.208	17.281 ± 0.083	16.840 ± 0.086	ARIES	
2014-05-17.63	795.13	125.40	—	19.404 ± 0.151	18.458 ± 0.193	17.367 ± 0.100	16.910 ± 0.088	ARIES	
2014-05-20.67	798.17	128.44	—	19.378 ± 0.158	18.660 ± 0.228	17.390 ± 0.087	17.014 ± 0.092	ARIES	
2014-05-21.67	799.17	129.44	—	19.452 ± 0.163	18.693 ± 0.234	17.406 ± 0.089	17.014 ± 0.093	ARIES	
2014-05-26.67	804.17	134.44	—	19.516 ± 0.203	18.606 ± 0.226	17.495 ± 0.117	17.122 ± 0.127	ARIES	
2014-05-29.68	807.18	137.45	—	19.542 ± 0.235	18.678 ± 0.272	17.509 ± 0.102	17.118 ± 0.109	ARIES	
2014-06-15.64	824.14	154.41	—	—	—	17.796 ± 0.156	17.417 ± 0.167	ARIES	
2014-06-16.63	825.13	155.40	—	—	18.918 ± 0.293	17.772 ± 0.148	17.430 ± 0.161	ARIES	
2014-06-27.65	836.15	166.42	—	20.092 ± 0.332	19.473 ± 0.501	18.014 ± 0.193	17.731 ± 0.225	ARIES	
2014-11-26.95	988.45	318.72	—	—	—	19.883 ± 0.959	19.792 ± 1.411	ARIES	

*Swift* UVOT photometry

UT Date (yyyy/mm/dd)	JD 2456000+	Phase <sup>a</sup> (day)	<i>uvw2</i> (mag)	<i>uvm2</i> (mag)	<i>uvw1</i> (mag)	<i>uvu</i> (mag)	<i>uvb</i> (mag)	<i>uvv</i> (mag)	Tel <sup>b</sup> /Inst
2014-01-15.76	673.26	1.45	14.019 ± 0.048	14.007 ± 0.048	13.845 ± 0.048	13.851 ± 0.044	15.032 ± 0.050	15.054 ± 0.067	SWIFT
2014-01-16.79	674.29	2.47	14.084 ± 0.048	—	13.803 ± 0.044	—	—	—	SWIFT
2014-01-17.19	674.69	2.87	14.115 ± 0.049	14.060 ± 0.054	13.789 ± 0.046	13.651 ± 0.043	14.786 ± 0.047	14.756 ± 0.068	SWIFT
2014-01-18.88	676.38	4.56	14.535 ± 0.054	14.326 ± 0.056	13.975 ± 0.048	13.655 ± 0.043	14.799 ± 0.047	14.568 ± 0.061	SWIFT
2014-01-19.21	676.71	4.89	14.610 ± 0.054	14.368 ± 0.056	13.987 ± 0.047	13.715 ± 0.043	14.765 ± 0.047	14.729 ± 0.061	SWIFT
2014-01-19.47	676.97	5.15	14.662 ± 0.053	—	—	13.725 ± 0.042	—	—	SWIFT
2014-01-20.80	678.30	6.48	14.954 ± 0.061	14.768 ± 0.064	14.223 ± 0.050	13.779 ± 0.043	14.767 ± 0.047	14.535 ± 0.059	SWIFT
2014-01-21.91	679.41	7.59	15.193 ± 0.069	15.038 ± 0.064	14.347 ± 0.052	13.850 ± 0.044	14.757 ± 0.047	14.601 ± 0.060	SWIFT
2014-01-22.96	680.46	8.65	15.474 ± 0.081	15.172 ± 0.069	14.675 ± 0.067	13.858 ± 0.045	14.692 ± 0.048	14.332 ± 0.058	SWIFT
2014-01-23.70	681.20	9.38	15.658 ± 0.087	—	—	13.949 ± 0.043	—	—	SWIFT
2014-01-23.97	681.47	9.65	15.630 ± 0.088	15.463 ± 0.080	14.780 ± 0.073	13.969 ± 0.047	14.783 ± 0.050	14.356 ± 0.062	SWIFT
2014-01-24.87	682.37	10.55	15.829 ± 0.078	15.646 ± 0.066	14.855 ± 0.063	14.004 ± 0.044	14.786 ± 0.047	14.581 ± 0.058	SWIFT
2014-01-29.41	686.91	15.09	16.735 ± 0.087	16.591 ± 0.081	15.581 ± 0.066	14.470 ± 0.048	14.975 ± 0.048	14.596 ± 0.057	SWIFT
2014-02-07.85	696.35	24.53	18.389 ± 0.158	18.446 ± 0.157	17.035 ± 0.087	15.620 ± 0.068	15.520 ± 0.056	14.963 ± 0.059	SWIFT
2014-02-10.18	698.68	26.86	18.636 ± 0.175	18.946 ± 0.208	17.349 ± 0.097	15.884 ± 0.069	15.763 ± 0.060	15.030 ± 0.059	SWIFT

<sup>a</sup> with reference to the explosion epoch JD=2456669.7d<sup>b</sup> ARIES: 104cm Sampurnanand telescope and 130cm Devasthal fast optical telescope at ARIES, Nainital, India; SWIFT: *Swift* UVOT

Note: Data observed within 5 Hrs, are represented under single epoch observation.

**APPENDIX B: TABLES OF POLARIMETRY**

**Table B1.** Polarimetric evolution of SNe 2013hj and 2014G.

UT Date (yyyy-mm-dd)	JD 2456000+	Phase <sup>a</sup> (day)	Observed		ISP <sub>MW</sub> subtracted	
			$P_R$ (%)	$\theta_R$ (°)	$P_R$ (%)	$\theta_R$ (°)
SN 2013hj						
2014-01-02.96	660.46	23.46	$0.56 \pm 0.42$	$132.3 \pm 21.8$	$0.63 \pm 0.42$	$127.3 \pm 21.8$
2014-01-07.83	665.33	28.33	$0.67 \pm 0.50$	$127.1 \pm 18.6$	$0.75 \pm 0.50$	$123.4 \pm 18.6$
2014-01-24.85	682.35	45.35	$0.44 \pm 0.21$	$150.8 \pm 10.4$	$0.44 \pm 0.21$	$142.5 \pm 10.4$
2014-02-05.73	694.23	57.23	$0.88 \pm 0.29$	$151.2 \pm 9.6$	$0.87 \pm 0.29$	$147.0 \pm 9.6$
2014-03-06.69	723.19	86.19	$0.98 \pm 0.43$	$128.8 \pm 12.8$	$1.07 \pm 0.43$	$126.1 \pm 12.8$
SN 2014G						
2014-01-23.92	681.42	11.72	$0.82 \pm 0.65$	$131.9 \pm 24.7$	$0.78 \pm 0.65$	$134.0 \pm 24.7$
2014-01-26.93	684.43	14.73	$1.59 \pm 0.21$	$132.2 \pm 4.2$	$1.54 \pm 0.21$	$133.3 \pm 4.2$
2014-02-05.82	694.32	24.62	$0.86 \pm 0.20$	$134.3 \pm 6.8$	$0.82 \pm 0.20$	$136.4 \pm 6.8$

<sup>a</sup> with reference to the explosion epochs JD 2456637.0d and 2456669.7d for SNe 2013hj and 2014G respectively.

**Table B2.** Polarization measurements in *R*-band for field stars towards the direction of SNe 2013hj and 2014G.

Star ID	$\alpha_{J2000}$ (h m s)	$\delta_{J2000}$ (° ' ")	$P_R$ (%)	$\theta_R$ (°)
Stars towards SN 2013hj.				
HD 80083	09:17:36.04	-07:27:46.44	$0.12 \pm 0.10$	$5.3 \pm 25.3$
HD 79289	09:12:47.60	-16:47:58.57	$0.16 \pm 0.07$	$10.0 \pm 15.1$
HD 79308	09:12:57.26	-15:25:09.56	$0.07 \pm 0.09$	$36.4 \pm 40.1$
HD 82734	09:33:12.46	-21:06:56.60	$0.25 \pm 0.07$	$18.8 \pm 8.0$
HD 80749	09:21:09.59	-15:31:37.92	$0.17 \pm 0.10$	$15.1 \pm 18.7$
HD 78891	09:10:10.34	-16:51:45.40	$0.03 \pm 0.05$	$18.7 \pm 42.9$
HD 79914	09:16:27.54	-13:50:02.81	$0.08 \pm 0.06$	$17.6 \pm 21.3$
HD 78920	09:10:24.80	-14:54:00.65	$0.05 \pm 0.05$	$12.1 \pm 35.3$
HD 77935	09:05:02.23	-11:23:15.73	$0.15 \pm 0.09$	$19.1 \pm 18.1$
HD 78954	09:10:35.01	-16:58:20.89	$0.05 \pm 0.06$	$27.1 \pm 30.7$
HD 80990	09:22:34.28	-16:54:15.12	$0.19 \pm 0.09$	$16.3 \pm 13.6$
Stars towards SN 2014G.				
HD 91480	10:35:09.69	+57:04:57.49	$0.32 \pm 0.08$	$17.7 \pm 8.7$
HD 94247	10:53:34.45	+54:35:06.46	$0.11 \pm 0.06$	$117.1 \pm 17.1$
HD 102328	11:46:55.62	+55:37:41.48	$0.22 \pm 0.07$	$95.4 \pm 8.9$